**Doctoral Dissertation**

# Control of Plasmonic Chiroptical Properties by the Design of Gold Nanostructures

(金ナノ粒子の構造設計による
プラズモンキラリティの制御)

**Han LIN**

**Doctor of Soft Matter Science**

**Division of Soft Matter**

**Graduate School of Life Science**

**Hokkaido University**

**March 2024**

# Table of Contents

## Acknowledgements

This doctoral thesis was conducted under the guidance of Associate Professor Hideyuki MITOMO and Professor Kuniharu IJIRO from RIES, Hokkaido University. I would like to express my profound gratitude to them for their unwavering support, mentorship and assistance throughout my doctoral studies. Their expertise, patience and encouragement have played a pivotal role in my academic development.

My sincere thanks to Professor Zhiyong GUO from Ningbo University for his strong supports in my research. Additionally, I appreciate the insightful discussions on my research conducted with Assistant Professor Yusuke YONAMINE from RIES, Hokkaido University.

Special thanks to the members of the Molecular Devices Laboratory, Special Assistant Professor Satoshi Nakamura, Postdoc Takehiro Yachi, Ms. Chie Takeuchi, Ms. Aki Okuhara, Dr. MBA Joshua Chidiebere, Dr. Kun Xiong, Mr. Yu Sekizawa, Ms. Melda Taspika, Ms. Jingyan Yang, Ms. Yali Shi, Mr. Ryo Sugiyama, Ms. Wenting Wei, Ms. Zhiyu He, Mr. Yingqi Mu, Mr. Tianxu Gao, Mr. Dongyu Zhang, Mr. Haoran Zhang, Mr. Abdul Kaiyum, Mr. Zirui Jiang, Ms. Chisato Toyokawa, Mr. Weijie Cheah, Mr. Kaito Shishido, Ms. Yuka Hasegawa, Ms. Honoka Niwa, Ms. Honoka Watanabe, Mr. Tomoki Ikemizu, Ms. Mio Nakamura, Ms. Hono Ogihara, Ms. Erika Kurimoto, for their camaraderie and stimulating academic environment. The collective effort and dedication of our group made a significant contribution to the completion of this study.

I want to express my deepest appreciation to my girlfriend Ms. Wenting Wei and my family for their continuous encouragement, understanding, and love. Their unwavering support has been my anchor throughout this demanding academic pursuit.

I acknowledge the financial support provided by China Scholarship Council that made this research possible. This assistance has been instrumental in facilitating the successful completion of my doctoral studies.

I extend my heartfelt gratitude to all those who have played a role in shaping my academic journey. Your support, encouragement, and belief in my abilities have been instrumental in reaching this significant milestone.

***Han LIN***

# *Chapter 1*

## *General Introduction*

## 1.1 Chirality

Chirality characterizes a geometric structure whose mirror image cannot be completely superimposed onto the original structure through translation or in-plane rotation.[1] This property is prevalent in nature across various length scales, ranging from the conformation of amino acids to the spirals of snail shells, and even to the morphologies of galaxies (**Figure 1.1**).[2] Although substances exhibiting chirality (referred to as enantiomers) generally manifest similar physical properties, their optical properties exhibit significant distinctions. Louis Pasteur first proposed a rational explanation for the optical activity and the relationship between structure and chirality in 1848.[3] Specifically, materials with chiral features display differences in the absorption of left- or right-circularly polarized (LCP or RCP) light, a phenomenon known as circular dichroism (CD).[4]

Based on this distinctive feature, the chiroptical response of biomolecules has become a valuable tool for understanding and distinguishing spatial configurations, particularly in the fields of stereochemistry, biology, pharmacology, and toxicology.[5-8] However, due to the relatively small volume of electromagnetic interactions, the chiroptical response of biomolecules is inherently weak, thereby constraining its further applications.[9]


**Figure 1.1** Chiral architectures in nature at various scales, from enantiomeric molecule at sub-nanometer scale to DNA and enzyme at nanometer scale, further to snail shells at living system and galaxy at macroscopic scale.[10]

## 1.2 Optical Properties of Gold Nanoparticles

Gold has long accompanied the evolution of human civilization in various forms. During the Middle Ages, colloidal solutions of gold nanoparticles (Au NPs) gained prominence as pigments for colored glass due to their intense color.[11] Eventually, they were crafted into works of art associated with royalty and religion, carrying profound symbolic significance. The Roman chalice (also known as the Lycurgus cup) serves as a notable example, displaying dichroic quality (**Figure 1.2A**).[12] When illuminated externally, the cup exhibits an emerald green color, while internal illumination reveals a wine-red hue. Additionally, the rose windows of the Notre-Dame Cathedral in Paris stand out as another significant instance, with the vibrant red and purple attributed to the presence of Au NPs (**Figure 1.2B**). The genesis of these artworks is intricately linked to the optical effects of Au NPs.[13]

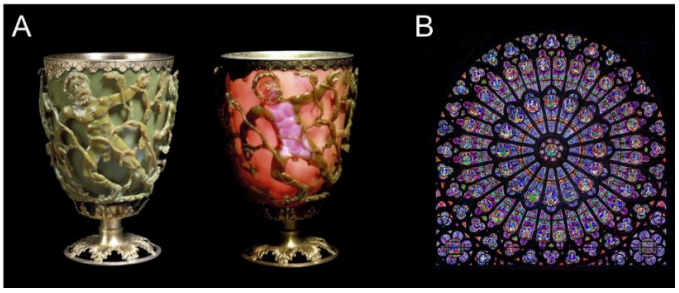


**Figure 1.2** (A) Photograph of the Lycurgus cup in reflected light (left) and transmitted light (right).[12] (B) Rose window of the Notre-Dame Cathedral in Paris.[13]

Until 1908, Gustav Mie provided the first rigorous mathematical description of the optical behavior of colloidal scattered light.[14] According to his theory, Au NPs possess a significant number of free-conducting and easily polarizable electrons, primarily distributed on their surface, which is an important prerequisite for their interaction with the electromagnetic field. The outcome of this interaction results in coherent oscillations of the free electron cloud on the particle surface, known as localized surface plasmon resonance (LSPR).[15] The wavelength of these oscillations is influenced by the size, shape, and material of the particles, significantly affecting the absorption and scattering behaviors of the particles, thereby generating noteworthy optical characteristics.[16]

Gold nanospheres (Au NSs) are the most extensively studied traditional Au NPs.[17, 18] However, due to the perfect geometric symmetry of their shape, their LSPR response is confined to the visible light range, and their sensitivity and tunability are relatively limited (**Figure 1.3A**).[19-21] Since the 1990s, numerous studies have focused on the development of anisotropic particles. Gold nanorods (Au NRs) have garnered significant attention due to their unique anisotropic plasmonic properties, widely tunable plasmon wavelengths, and excellent reproducibility.[22, 23] Owing to their structural anisotropy, Au NRs exhibit two LSPR modes, namely, transverse mode (T-LSPR) and longitudinal mode (L-LSPR). With an increase in aspect ratio, the longitudinal dipole plasmon wavelength of Au NRs linearly increases, covering the visible to infrared range (**Figure 1.3B**).[24]

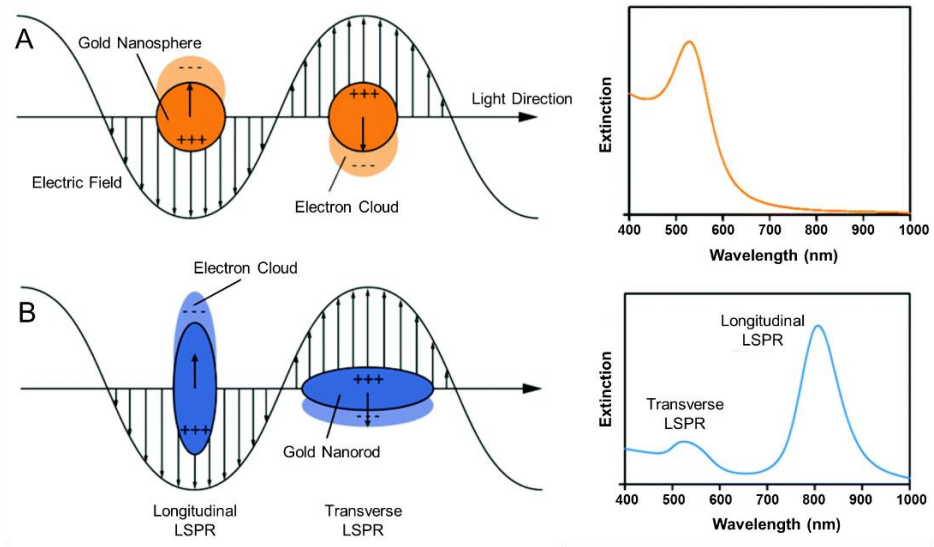


**Figure 1.3** Scheme of the surface plasmon oscillation and extinction spectra for (A) Au NSs and (B) Au NRs.[25]

Under resonance excitation, Au NPs possess a unique capability to concentrate the free-space optical field near their surfaces, forming an enhanced electric field around the particles.[26] This electric field, through novel mechanisms, can generate various interactions between light and matter, such as plasmon-enhanced spectroscopy, optical nanoantenna, photothermal conversion, and plasmon-assisted photochemical reactions.[27-30] Driven by these captivating optical properties, LSPR has emerged as a thriving and burgeoning field in the realms of science and technology.

## 1.3 Chiroptical Properties of Chiral Gold Nanoparticles

With the latest advancements in nanofabrication technologies, the field of chiral research has expanded beyond traditional chiral molecules to larger-scale chiral Au NPs.[31] The properties of LSPR bestow upon these particles chiroptical activity and enhanced optical responses in the visible and even near-infrared regions.[32] These characteristics render chiral Au NPs active in various domains, including biosensing, chiral catalysis, polarization tuning, chiroptical detection.[33-36]

Preparing chiral metal nanostructures primarily involve two strategies: top-down and bottom-up approaches. The top-down strategy, represented by emerging technologies such as electron beam lithography, oblique angle deposition, and direct laser writing, provides pathways to integrate chiral structures into plasmonic materials.[37-39] On the other hand, the bottom-up strategy, exemplified by chiral ligand-assisted colloid particle synthesis and self-assembly, demonstrates several advantages, including nanoscale precision control, large-scale parallel production, ease of storage, transferability, and cost-effectiveness.[40] Over the past decade, efforts have gradually transitioned from enhancing chiroptical activity to unveiling the mechanisms underlying chirality generation.

Two distinct physical mechanisms leading to the unique chiral response of metal particles have been observed,[41] including: 1) chiral transfer from chiral molecules to achiral NPs. Chiral molecules in the vicinity of achiral NPs have the capability to induce chiral currents on the NP surface, leading to a novel CD response in the proximity of plasmonic resonances (plasmon-induced chirality, **Figure 1.4A**). This phenomenon is grounded in the mutual coupling between the molecular exciton and the particle plasmon, facilitating the transference of chiral features to visible wavelengths (**Figure 1.4B**); 2) assembling achiral NPs into an ordered chiral arrangement, followed by inducing chiroptical effects through interparticle Coulomb interactions (plasmonic chirality, **Figure 1.4C**). Depending on the spatial orientation of the arrangement, this interaction further categorizes plasmon resonances into collective bonding and anti-bonding modes (**Figure 1.4D**).

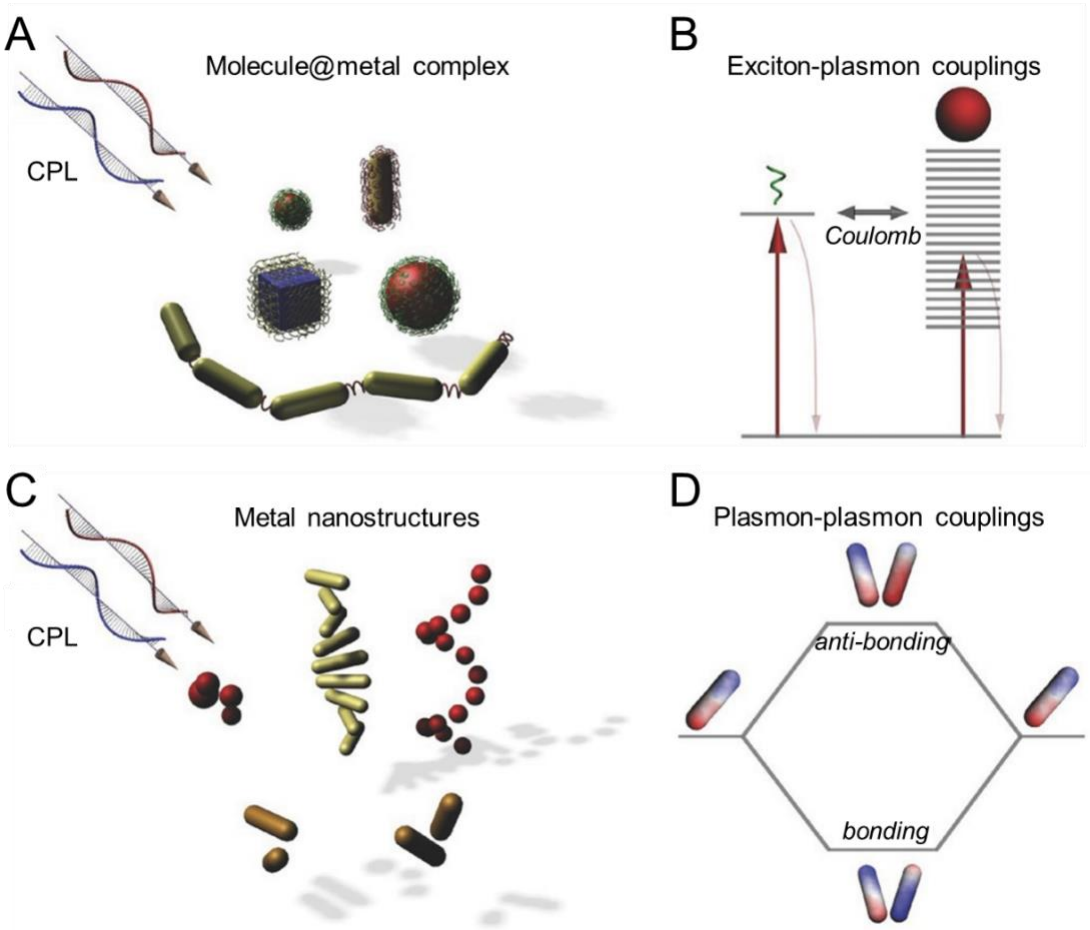


**Figure 1.4** (A) Models of chiral-molecule/metal NPs complexes including chiral molecules covered metal NPs and chains. (B) Model of exciton-plasmon interaction in a chiral molecule/Au NP complex. The chiral molecule is excited by the incident photons and plays the role of a molecule dipole. This molecule dipole can couple with the surface plasmons of a Au NP through Coulombic interactions, and therefore transfer its molecular chirality to the Au NP. (C) Examples of chiral arrangements of metal NPs, including Au NP tetramers and helixes, and Au NR dimers and helixes. (D) The typical plasmon-plasmon coupling in a Au NR dimer, where bonding and anti-bonding plasmon modes are formed through plasmon hybridization. The positive and negative charges on the Au NR surface are modeled in red and blue.[41]

The key point is that the mechanisms mentioned above indicate the potential for bottom-up techniques to regulate the generated chiroptical responses. This enriches the opportunities for realizing chiral switches, tunable optical films, and highly sensitive detection.[40]

## 1.4 Active Chiral Plasmonics

The term "active chiral plasmonics" can be viewed as an evolution stemming from active plasmonics.[42] In contrast to the dynamic control focusing solely on surface plasmon resonance, the chiroptical activity tuning of active chiral plasmonics offers a more diverse range of modulation channels, including changes or reversals in signal intensity, as well as wavelength shifts.[43] However, active chiral plasmonics also pose more formidable challenges in terms of target structures, external environments, and operational precision. This is because the generation of chiral responses strictly depends on the state of chiral ligands or the spatial geometric parameters of chiral plasmonic components.[31] However, it is undeniable that research and development on active plasmonics offer valuable reference suggestions for the in-depth exploration of active chiral plasmonics.

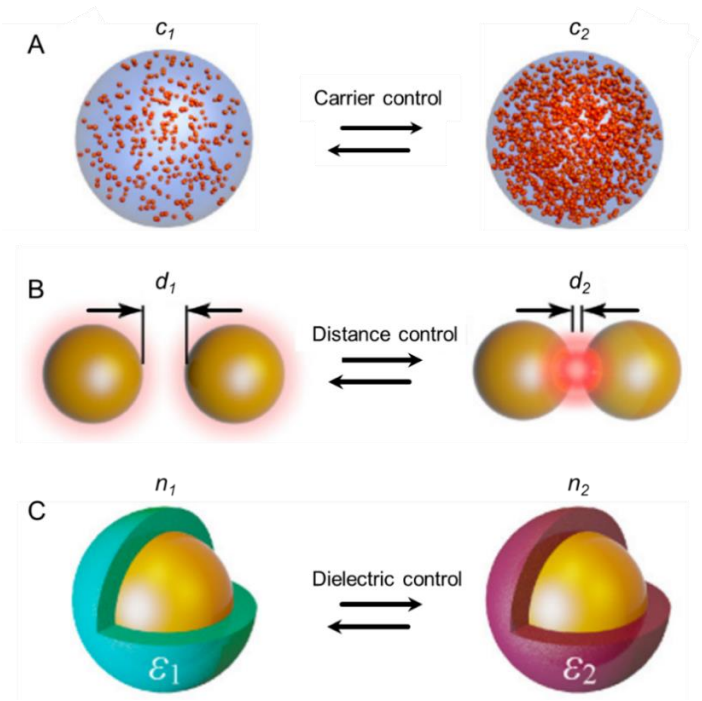


**Figure 1.5** (A) Self-tunable plasmonic structures. The red ball is the model for carriers in the plasmonic. $c_1$ and $c_2$ represent the carrier density change before and after. (B) Plasmonic structures with tunable gap distances. $d_1$ and $d_2$ represent the gap distance change before and after. (C) Plasmonic structures within tunable dielectric environments. The green ($\varepsilon_1$) and purple ($\varepsilon_2$) shells are different mediums. $n_1$ and $n_2$ represent the refractive index change before and after.[44]

According to the LSPR modulation mechanisms, three categories of active plasmonic structures have been proposed,[44] including: 1) self-tunable plasmonic structures, achieved by inducing variations in the carrier density and dielectric functionality of the plasmonic material itself, thereby enabling active control the LSPR behaviors (**Figure 1.5A**); 2) plasmonic structures with tunable gap distances, whose plasmonic response relies on the sensitivity of plasmonic coupling effects to the interparticle gap distance (**Figure 1.5B**); 3) plasmonic structures within tunable dielectric environments, where the modulation performance is largely contingent upon the properties of the surrounding tunable medium (**Figure 1.5C**). The corresponding structures cover discrete particles and assemblies.

To date, research on the reconfigurable active chiral plasmonic nanostructures has predominantly focused on dimers or three-dimensional assemblies.[45-47] This is attributed to the extensive development of stimuli-responsive templates, notably with the introduction of DNA origami technology.[48] This technique facilitates the programming and creation of intricate spatially chiral plasmonic structures. Furthermore, it allows for conformational changes under DNA control at the nanoscale, thereby manifesting an immediate dynamic chiroptical response. However, this strategy typically relies on a liquid environment and incurs higher costs, posing challenges for further industrialization and widespread adoption.

On the other hand, there have been very few reports on the dynamically tunable plasmonic chiroptical activities of discrete metal NPs, especially in wavelength shifts, mainly due to the vulnerability of most chiral molecules to external stimuli and the instability of the metal NPs and their unadjustable LSPR wavelength ($\lambda_{LSPR}$).[49] Moreover, it is noteworthy that the plasmon-induced chiroptical activity tends to exhibit relatively weak intensity, serving as one of the limiting factors in the development of dynamic tuning.[50] Dynamic modulation becomes meaningful only when a substantial chiroptical response intensity is achieved.

In general, one of the current bottlenecks in the research on active chiral plasmonics is how to effectively amplify and dynamically control the chiroptical activities of discrete metal NPs.[51]

## 1.5 Aims of this Project

Designing and fabricating plasmonic chiral structures through the chiral units or chiral assembly of achiral units constitute an extraordinarily dynamic research domain. This dynamism is particularly evident in the rapid advancements seen in the construction of blocks, templates, and strategies in recent years. Presently, research interests in this field have progressively shifted towards amplifying and dynamically controlling chiroptical activity. This is driven by the requirements of future applications in nanophotonics and sensing, necessitating switchable and adaptive chiral responses. However, in this research process, there are still numerous unresolved issues. One key challenge is the lack of developed effective strategies for amplifying and tuning the chiroptical activity of discrete plasmonics.

In this project, I presented an open platform for discrete active chiral plasmonics fabrication that allowed for the flexible and rational customization of plasmonic cores, chiral molecules, and variable dielectrics according to the requirements of chiroptics. Additionally, in the pursuit of discrete plasmonic NPs with enhanced chiroptical activities, I explored the fabrication of gold octahedral nanoframes with chiral morphologies. A brief description of each chapter follows,

Chapter 1: A general introduction to chiral plasmonics as well as active chiral plasmonics was given.

Chapter 2: A discrete chiral core-gap-shell nanoparticle was prepared, with its plasmon-induced chirality amplified by the intragap hot-spots.

Chapter 3: The chiroptical activity of chiral nanoparticles exhibited dual modulation to pH and electric potential after coating with a polyaniline layer.

Chapter 4: An exploration of the synthesis of gold octahedral nanoframes with chiral morphology.

Chapter 5: A summary of the work as well as an outlook.

## 1.6 References


[1] Prelog, V. Chirality in Chemistry. *Science* **1976**, *193*, 17-24.

[2] Ulbricht, T. L. V. Chirality and Origin of Life. *Nature* **1975**, *258*, 383-384.

[3] Pasteur, L. Sur Les Relations Qui Peuvent Exister Entre La Forme Crystalline, La Composition Chimique et Le Sens de La Polarization Rotatoire. *Ann. Chim. Phys.* **1848**, *24*, 442-459.

[4] Davis, W. B.; Svec, W. A.; Ratner, M. A.; Wasielewski, M. R. Molecular-Wire Behaviour in p-Phenylenevinylene Oligomers. *Nature* **1998**, *396*, 60-63.

[5] Yang, C.; Li, Y.; Zhou, S. Guo, Y.; Jia, C.; Liu, Z.; Houk, K. N.; Dubi, Y.; Guo, X.; Real-Time Monitoring of Reaction Stereochemistry through Single-Molecule Observations of Chirality-Induced Spin Selectivity. *Nat. Chem.* **2023**, *15*, 972-979.

[6] Glavin, D. P.; Burton, A. S.; Elsila, J. E.; Aponte, J. C.; Dworkin, J. P. The Search for Chiral Asymmetry as a Potential Biosignature in our Solar System. *Chem. Rev.* **2020**, *120*, 4660-4689.

[7] Nguyen, L. A.; He, H.; Pham-Huy, C. Chiral Drugs: An Overview. *Int. J. Biol. Sci.* **2006**, *2*, 85-100.

[8] Ye, J.; Zhao, M.; Niu, L.; Liu, W. Enantioselective Environmental Toxicology of Chiral Pesticides. *Chem. Res. Toxicol.* **2015**, *28*, 325-338.

[9] Kong, X. T.; Besteiro, L. V.; Wang, Z.; Govorov, A. O. Plasmonic Chirality and Circular Dichroism in Bioassembled and Nonbiological Systems: Theoretical Background and Recent Progress. *Adv. Mater.* **2020**, *32*, 1801790.

[10] Zhang, G.; Cheng, X.; Wang, Y.; Zhang, W. Supramolecular Chiral Polymeric Aggregates: Construction and Applications. *Aggregate* **2023**, *4*, e262.

[11] Montanarella, F.; Kovalenko, M. V. Three Millennia of Nanocrystals. *ACS Nano* **2022**, *16*, 5085-5102.

[12] Harden, D. B.; Toynbee, J. M. C. VII.—The Rothschild Lycurgus Cup. *Archaeologia* **1959**, *97*, 179-212.

[13] Cardell, C.; Guerra, I. Natural Corrosion-Induced Gold Nanoparticles Yield Purple Color of Alhambra Palaces Decoration. *Sci. Adv.* **2022**, *8*, 1-8.

[14] Mie, G. Beiträge Zur Optik Trüber Medien, Speziell Kolloidaler Metallösungen. *Annalen der Physik* **1908**, *330*, 377-445.

[15] Hutter, E.; Fendler, J. H. Exploitation of Localized Surface Plasmon Resonance. *Adv. Mater.* **2004**, *16*, 1685-1706.

[16] Burda, C.; Chen, X.; Narayanan, R.; El-Sayed, M. A. Chemistry and Properties of Nanocrystals of Different Shapes. *Chem. Rev.* **2005**, *105*, 1025-1102.

[17] Turkevich, J.; Stevenson, P. C.; Hillier, J. A Study of the Nucleation and Growth Processes in the Synthesis of Colloidal Gold. *Discuss. Faraday Soc.* **1951**, *11*, 55-75.

[18] Frens, G. Controlled Nucleation for Regulation of Particle-Size in Monodisperse Gold Suspensions. *Nature, Phys. Sci.* **1973**, *241*, 20-22.

[19] Amendola, V.; Pilot, R.; Frasconi, M.; Maragò, O. M.; Iatì, M. A. Surface Plasmon Resonance in Gold Nanoparticles: A Review. *J. Phys.: Condens. Matter* **2017**, *29*, 203002.

[20] Garcia, M. A. Surface Plasmons in Metallic Nanoparticles: Fundamentals and Applications. *J. Phys. D: Appl. Phys.* **2011**, *44*, 283001.

[21] Jang, H. J.; Ham, S.; Acapulco, J. A., Jr.; Song, Y.; Hong, S.; Shuford, K. L.; Park, S. Fabrication of 2D Au Nanorings with Pt Framework. *J. Am. Chem. Soc.* **2014**, *136*, 17674-17680.

[22] Chen, H. J.; Shao, L.; Li, Q.; Wang, J. F. Gold Nanorods and Their Plasmonic Properties. *Chem. Soc. Rev.* **2013**, *42*, 2679-2724.

[23] Zheng, J.; Cheng, X.; Zhang, H.; Bai, X.; Ai, R.; Shao, L.; Wang, J. Gold Nanorods: The Most Versatile Plasmonic Nanoparticles. *Chem. Rev.* **2021**, *121*, 13342-13453.

[24] Wang, G.; Akiyama, Y.; Kanayama, N.; Takarada, T.; Maeda, M. Directed Assembly of Gold Nanorods by Terminal-Base Pairing of Surface-Grafted DNA. *Small* **2017**, *13*, 1702137.

[25] Maturi, M.; Locatelli, E.; Monaco, I.; Franchini, M. C. Current Concepts in Nanostructured Contrast Media Development for in Vivo Photoacoustic Imaging. *Biomater. Sci.* **2019**, *7*, 1746-1775.

[26] Kim, J.-M.; Lee, C.; Lee, Y.; Lee, J.; Park, S.-J.; Park, S.; Nam, J.-M. Synthesis, Assembly, Optical Properties, and Sensing Applications of Plasmonic Gap Nanostructures. *Adv. Mater.* **2021**, 2006966.

[27] Li, J.-F.; Zhang, Y.-J.; Ding, S.-Y.; Panneerselvam, R.; Tian, Z.-Q. Core-Shell Nanoparticle-Enhanced Raman Spectroscopy. *Chem. Rev.* **2017**, *117*, 5002-5069.

[28] Giannini, V.; Fernandez-Dominguez, A. I.; Heck, S. C.; Maier, S. A. Plasmonic Nanoantennas: Fundamentals and Their Use in Controlling the Radiative Properties of Nanoemitters. *Chem. Rev.* **2011**, *111*, 3888-3912.

[29] Jauffred, L.; Samadi, A.; Klingberg, H.; Bendix, P. M.; Oddershede, L. B. Plasmonic Heating of Nanostructures. *Chem. Rev.* **2019**, *119*, 8087-8130.

[30] Zhan, C.; Chen, J. X.; Yi, J.; Li, F. J.; Wu, D. Y.; Tian, Z. Q. From Plasmon-Enhanced Molecular Spectroscopy to Plasmon Mediated Chemical Reactions. *Nat. Rev. Chem.* **2018**, *2*, 216-230.

[31] Urban, M. J.; Shen, C.; Kong, X.-T.; Zhu, C.; Govorov, A. O.; Wang, Q.; Hentschel, M.; Liu, N. Chiral Plasmonic Nanostructures Enabled by Bottom-Up Approaches. *Annu. Rev. Phys. Chem.* **2019**, *70*, 275-299.

[32] Hentschel, M.; Schäferling, M.; Duan, X.; Giessen, H.; Liu, N. Chiral Plasmonics. *Sci. Adv.* **2017**, *3*, e1602735.

[33] Ma, W.; Xu, L.; Wang, L.; Xu, C.; Kuang, H. Chirality-Based Biosensors. *Adv. Funct. Mater.* **2019**, *29*, 1805512.

[34] Bainova, P.; Joly, J. P.; Urbanova, M.; Votkina, D.; Erzina, M.; Vokata, B.; Trelin, A.; Fitl, P.; Audran, G.; Vanthuyne, N.; Vinklarek, J.; Svorcik, V.; Postnikov, P.; Marque, R. A. S.; Lyutakov, O. Plasmon-Assisted Chemistry Using Chiral Gold Helicoids: Toward Asymmetric Organic Catalysis. *ACS Catal.* **2023**, *13*, 12859-12867.

[35] Cai, J.; Zhang, W.; Xu, L.; Hao, C.; Ma, W.; Sun, M.; Wu, X.; Qin, X.; Colombari, F. M.; Farias de Moura, A.; Xu, J.; Silva, M. S.; Carneiro-Neto, E. B.; Gomes, W. R.; Vallée, R. A. L.; Pereira, E. C.; Liu, X.; Xu, C.; Klajn, R.; Kotov, N. A.; Kuang, H. Polarization-Sensitive Optoionic Membranes from Chiral Plasmonic Nanoparticles. *Nat. Nanotechnol.* **2022**, *17*, 408-416.

[36] Liu, Z.; Ai, J.; Kumar, P.; You, E.; Zhou, X.; Liu, X.; Tian, Z.; Bouř, P.; Duan, Y.; Han, L.; Kotov, N. A.; Ding, S.; Che, S. Enantiomeric Discrimination by Surface-Enhanced Raman Scattering-Chiral Anisotropy of Chiral Nanostructured Gold Films. *Angew. Chem. Int. Ed.* **2020**, *59*, 15226-15231.

[37] Hentschel, M.; Karst, J.; Giessen, H. Tailored Optical Functionality by Combining Electron-beam and Focused Gold-ion Beam Lithography for Solid and Inverse Coupled Plasmonic Nanostructures. *Adv. Opt. Mater.* **2020**, *8*, 2000879.

[38] Hou, Y.; Leung, H. M.; Chan, C. T.; Du, J.; Chan, H. L. W.; Lei, D. Y. Ultrabroadband Optical Superchirality in a 3D Stacked-Patch Plasmonic Metamaterial Designed by Two-Step Glancing Angle Deposition. *Adv. Funct. Mater.* **2016**, *26*, 7807-7816.

[39] Sakellari, I.; Yin, X.; Nesterov, M. L.; Terzaki, K.; Xomalis, A.; Farsari, M. 3D Chiral Plasmonic Metamaterials Fabricated by Direct Laser Writing: The Twisted Omega Particle. *Adv. Opt. Mater.* **2017**, *5*, 1-6.

[40] Probst, P. T.; Dong, Y.; Zhou, Z.; Aftenieva, O.; Fery, A. Bottom-Up Assembly of Inorganic Particle-Based Chiroptical Materials. *Adv. Opt. Mater.* **2023**, 2301834.

[41] Lan, X.; Wang, Q. Self-Assembly of Chiral Plasmonic Nanostructures. *Adv. Mater.* **2016**, *28*, 10499-10507.

[42] Yin, X.; Schäferling, M.; Michel, A.-K. U.; Tittl, A.; Wuttig, M.; Taubner, T.; Giessen, H. Active Chiral Plasmonics. *Nano Lett.* **2015**, *15*, 4255-4260.

[43] Jeong, H.-H.; Mark, A. G.; Alarcón-Correa, M.; Kim, I.; Oswald, P.; Lee, T.-C.; Fischer, P. Dispersion and Shape Engineered Plasmonic Nanosensors. *Nat. Commun.* **2016**, *7*, 11331.

[44] Jiang, N.; Zhuo, X.; Wang, J. Active Plasmonics: Principles, Structures, and Applications. *Chem. Rev.* **2018**, *118*, 3054-3099.

[45] Lv, J.; Gao, X.; Han, B.; Zhu, Y.; Hou, K.; Tang, Z. Self-assembled Inorganic Chiral Superstructures. *Nat. Rev. Chem.* **2022**, *6*, 125-145.

[46] Lee, H.-E.; Ahn, H.-Y.; Lee, J.; Nam, K. T. Biomolecule-Enabled Chiral Assembly of Plasmonic Nanostructures. *ChemNanoMat* **2017**, *3*, 685-697.

[47] Zhou, S.; Li, J.; Lu, J.; Liu, H.; Kim, J.-Y.; Kim, A.; Yao, L.; Liu, C.; Qian, C.; Hood, Z. D.; Lin, X.; Chen, W.; Gage, E.; Arslan, I.; Travesset, A.; Sun, K.; Kotov, N. A.; Chen, Q. Chiral Assemblies of Pinwheel Superlattices on Substrates. *Nature* **2022**, *612*, 259-265.

[48] Zhou, C.; Duan, X.; Liu, N. DNA-Nanotechnology-Enabled Chiral Plasmonics: From Static to Dynamic. *Acc. Chem. Res.* **2017**, *50*, 2906-2914.

[49] Lin, H.; Song, L.; Huang, Y.; Cheng, Q.; Yang, Y.; Guo, Z.; Su, F.; Chen, T. Macroscopic Au@PANI Core/Shell Nanoparticle Superlattice Monolayer Film with Dual-Responsive Plasmonic Switches. *ACS Appl. Mater. Interfaces* **2020**, *12*, 11296-11304.

[50] Xu, L.; Wang, X.; Wang, W.; Sun, M.; Choi, W. J.; Kim, J. Y.; Hao, C.; Li, S.; Qu, A.; Lu, M.; Wu, X.; Colombari, F. M.; Gomes, W. R.; Blanco, A. L.; de Moura, A. F.; Guo, X.; Kuang, H.; Kotov, N. A.; Xu, C. Enantiomer-Dependent Immunological Response to Chiral Nanoparticles. *Nature* **2022**, *601*, 366-373.

[51] Nguyen, M.-K.; Kuzyk, A. Reconfigurable Chiral Plasmonics beyond Single Chiral Centers. *ACS Nano* **2019**, *13*, 13615-13619.

# *Chapter 2*

## *Enhancement of Plasmonic Chiroptical Properties by Construction of Interparticle Gaps*

## 2.1 Introduction

Recent studies have demonstrated an interesting form of coupling between chiral molecules and metal nanoparticles, which is associated with the LSPR phenomenon, the strong electromagnetic field of which is able to enhance the CD signals of surface chiral molecules.[1-5] Meanwhile, chiral molecules can also induce dissipative chiral currents arising inside the particles and provide the feedback of a new CD response near the LSPR position of the particles. This effect is termed plasmon-induced chirality, $CD_{LSPR}$ or $CD_{plasmon\text{-}induced}$.[6-8] This exciting phenomenon enables nanomaterials to further serve as circular polarizers, providing optical manipulation capabilities in areas such as enantioselective sensing, enantiomer separation, and photochemical or photothermal chiral applications.[9-12]

However, in practice, simply placing chiral molecules on the surface of metal nanoparticles results in a very weak $CD_{LSPR}$ response due to the correspondingly low local electromagnetic field intensity.[13, 14] Therefore, naturally, enhancing this local electromagnetic field intensity to significantly boost $CD_{LSPR}$ response has become the next challenge for researchers. An ideal strategy involves constructing plasmonic dimers or ordered assemblies to provide nanoscale or sub-nanoscale gaps, often accompanied by high-intensity electromagnetic fields, known as "hot-spots". This design is also commonly employed in the construction of surface-enhanced raman spectroscopy (SERS) platforms.[15] Our lab previously reported that active gap distance control using tunable plasmonic substrates can significantly intensify the SERS signals of proteins.[16]

Correspondingly, the initial study confirmed the crucial role of hot-spots in amplifying chiral responses through a theoretical model of dimers formed by perfect spherical particles.[17] Subsequently, one-dimensional (1D) assemblies composed of cysteine (Cys) molecules and Au NRs were employed to enhance $CD_{LSPR}$ responses. By adjusting the aspect ratio of the Au NRs in the one-dimensional assembly, the wavelength of the $CD_{LSPR}$ response was successfully tuned from 550 nm to above 900 nm.[18] Furthermore, the synergistic interaction between Cys molecules and

surfactants has been confirmed to adjust the assembly pattern of Au NRs, transitioning from end-to-end to side-by-side. The conformation-dependent nature of the corresponding $CD_{LSPR}$ response arises from changes in electromagnetic interactions between Au NRs within the assembly.[19] In recent studies, double-stranded DNA, serving as a chiral molecule, was positioned within plasmonic hot-spots formed by dimers. This system was also verified to significantly enhance the transfer effect of CD, especially between the ends of nanorods.[20]

In addition to interparticle gaps, constructing intraparticle gaps is also considered one of the most promising strategies due to its higher stability and reproducibility compared to assemblies. Correspondingly, one of the most extensively studied intraparticle nanostructures is the core–gap–shell structure, where a complete shell surrounds a core particle with a nanoscale internal gap.[21] For example, core-shell nanospheres (AuAg NSs) with internal nano gaps containing Cys molecules, it was confirmed that they amplified the corresponding plasmonic chiral response.[22] Alternatively, by using single-stranded DNA rich in cytosine as a template to guide the growth of a silver shell, a plasmonic CD signal was generated in the Au@Ag nanospheres. With an increase in the thickness of the Ag shell, the DNA-plasmon interaction could be further amplified through electromagnetic coupling in the core-shell structure.[23]

In this chapter, I demonstrate an enhanced plasmonic chiroptical system based on chiral core–gap–shell gold nanoparticles (c-CGS Au NPs). The Au NR used as a core was loaded with Cys molecules as a chiral source, forming a gap of sub-monolayer thickness by the regrowth of the Au shell. This gap structure with a natural electromagnetic field hot-spots significantly enhanced the $CD_{LSPR}$ response. Furthermore, experimental results indicate a significant correlation between the configuration and concentration of Cys molecules and $CD_{LSPR}$ response, as well as particle morphology. Particularly noteworthy is the induction of a well-defined $CD_{T\text{-}LSPR}$ from the initially less conspicuous T-LSPR in the extinction spectra, providing a potential avenue for the precise modulation of chiroptical activities.

## 2.2 Experimental Section

### Materials

Chloroauric acid ($HAuCl_4 \cdot 3H_2O$, 99.9%) were purchased from Sigma-Aldrich. Cetrimonium bromide (CTAB, >99.0%), hexadecyltrimethylammonium chloride (CTAC, ≥95.0%) were purchased from TCI (Shanghai). Sodium borohydride ($NaBH_4$, 99.0%), ascorbic acid (AA, 99.7%), silver nitrate ($AgNO_3$, >99.0%) and hydrochloric acid (HCl, 37 wt% in water) were obtained from Sinopharm Chemical Reagent Co., Ltd. (Shanghai). Sodium hypochlorite solution (NaClO, available chlorine 6–15%) was purchased from Aladdin.

### Characterization

UV−vis and CD spectra were recorded by a TU-1810 spectrophotometer (Purkinje General Instrument Co., Ltd.) and Jasco J-1700-150 spectropolarimeter, respectively. Field-emission scanning electron microscopy (FE-SEM) observation was carried out using an S-4800 instrument (Hitachi) at an acceleration voltage of 8 kV. Transmission electron microscopy (TEM) was performed on a JEM-2100F electron microscope operating at 200 kV.

### Preparation of Au NSs

CTAC-coated Au NSs were prepared according to the seed-mediated growth method.[24] First, Au seeds were prepared by injecting fresh ice-cold $NaBH_4$ aqueous solution (0.2 mL, 20 mM) into a mixture of $HAuCl_4$ (0.1 mL, 25 mM) and CTAC (5 mL, 0.1 M) solution with vigorous stirring for 3 min, and the mixture was let stand undisturbed for 30 min to allow the excess $NaBH_4$ to age out.

The resulting Au seed solution (90 μL) was injected into a mixture of AA (40 μL, 0.1 M) and CTAC (10 mL, 25 mM) and then stirred for 5 min. Next, $HAuCl_4$ solution (100 μL, 25 mM) was injected, stirred vigorously for 1 min, and incubated for 20 min to obtain the bigger Au seeds (diameter: 10 nm). Furthermore, growth was achieved by adding $HAuCl_4$ solution (200 μL, 25 mM) to a mixture of AA (80 μL, 0.1 M), CTAC (20 mL, 25 mM) and Au seeds (10 nm, 50 μL). After stirring vigorously for 30 s, the solution was let stand undisturbed for at least 1.5 h. The optimization of the

morphology of Au NSs was accomplished by a two-step oxidative etching. Specifically, a diluted NaClO solution (available chlorine 1–2.5%, 20 μL) was injected to neutralize the excess AA, and the mixture was stirred rapidly for 5 min to complete the first etching. The second etching was performed by adding $HAuCl_4$ (10 μL, 25 mM) to the above solution while stirring for 30 s. The mixture was then incubated for 1 h to obtain homogeneous Au NSs.

Finally, homogeneous CTAC-coated Au NSs (diameter: 50 nm) were redispersed in CTAC solution (100 mL, 80 mM) after centrifugation (3405*g*, 10 min).

### Preparation of Au NRs

CTAC-coated Au NRs were prepared according to the previously reported seed-mediated method.[25] First, the seed solution was prepared by rapid injection of fresh ice-cold $NaBH_4$ aqueous solution (0.6 mL, 10 mM) into a mixture of $HAuCl_4$ (0.1 mL, 25 mM) and CTAB (9.9 mL, 0.1 M) with vigorous stirring for 2 min. The color of the seed solution changed from yellow to brown. The seed solution was left undisturbed for at least 30 min before use.

The growth solution was prepared by mixing CTAB solution (200 mL, 0.1 M) with $AgNO_3$ solution (6 mL, 10 mM) and letting it stand undisturbed (30 °C, 15 min). $HAuCl_4$ solution (4 mL, 25 mM) was then added, and the mixture was stirred (700 rpm, 30 min). Subsequently, HCl (0.35 mL, 12.1 M) was added, and the mixture was stirred (400 rpm, 15 min). AA solution (1.6 mL, 0.1 M) was then added, and the mixture was stirred vigorously (1200 rpm, 30 s), followed by the injection of 20 μL of the above seed solution with vigorous stirring (1500 rpm, 30 s). The mixed solution was then left undisturbed to allow Au NR growth (30 °C, 12 h).

Finally, the resulting Au NRs were centrifuged (4448*g*, 10 min) and redispersed in CTAC solution (100 mL, 80 mM) twice for further use.

### Preparation of c-CGS Au NRs and c-CGS Au NSs

The c-CGS nanostructures consisted of a core (Au NRs or Au NSs), a gap (Cys) and a shell (gold shell), which were prepared as follows:

CTAC-coated Au NRs or Au NSs (250 μL) were injected into a mixture of $HAuCl_4$ (25 μL, 1 mM), CTAC (1 mL, 40 mM), AA (20 μL, 0.1 M), and L- or D-Cys

molecules with different concentrations (180 μL), shaken gently for 10 s, and incubated for 1 h at room temperature.

$HAuCl_4$ (25 μL, 10 mM) was injected to the above solution, shaken gently for 10 s, and incubated for 2 h. The final concentration of L- or D-Cys was maintained at 5, 50, and 500 nM, corresponding to products including c-CGS Au NRs (I), c-CGS Au NRs (II), and c-CGS Au NRs (III), respectively.

The above products were centrifuged (3405*g*, 10 min) and redispersed in CTAC solution (1.5 mL, 5 mM). To further confirm that the main chiral signal came from the encapsulated Cys molecules, c-CGS Au NRs were treated using $NaBH_4$ solution (100 μL, 40 mM) and re-dissolved in CTAC solution (1.5 mL, 40 mM) used for CD measurements because $NaBH_4$ could remove any thiols from the gold surface.

## Calculation of the g-Factor

The asymmetry factor of the polarization rotation, also known as the *g*-factor, is a concentration-independent parameter.[26] It is calculated as the ratio of the different absorbances of a substance between LCP light and RCP light to the total absorbance using the following equation.

$$g = \frac{CD\ (mdeg)}{32980 \cdot Abs}$$

## 2.3 Results and Discussion

### Characterization of Au NRs and L-/D-Cys

Au NRs were prepared using the previously reported seed-mediated method. Their average length of 110 nm, width of 40 nm, and aspect ratio of 2.75 were confirmed by TEM image (**Figure 2.1A**). The optical activities of the Au NRs solution were recorded using both extinction spectra and CD spectra. The T-LSPR peak of Au NRs located at 520 nm and the L-LSPR peak located near 720 nm (**Figure 2.1B**), however, no significant CD peaks were observed, as no chiral factors were introduced into the environment (**Figure 2.1C**). The L- and D-Cys solutions showed extinction peaks located in the UV region (near 200 nm) and corresponding opposite CD peaks due to the presence of chiral centers in their chemical structures (**Figure 2.2**).

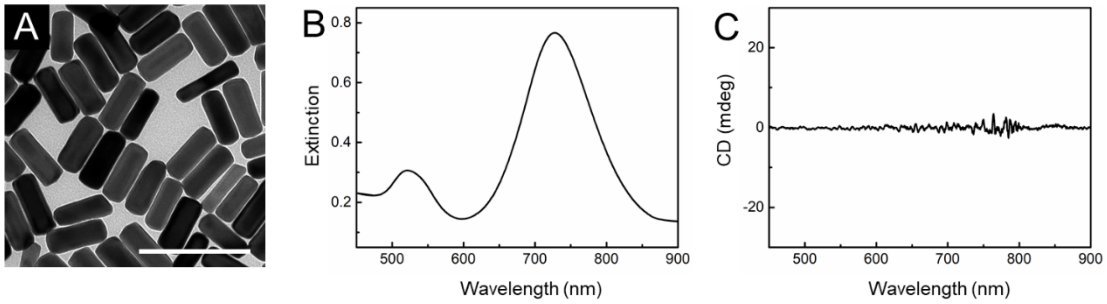


**Figure 2.1** (A) TEM image, (B) extinction and (C) CD spectra of Au NRs. The scale bar is 200 nm.

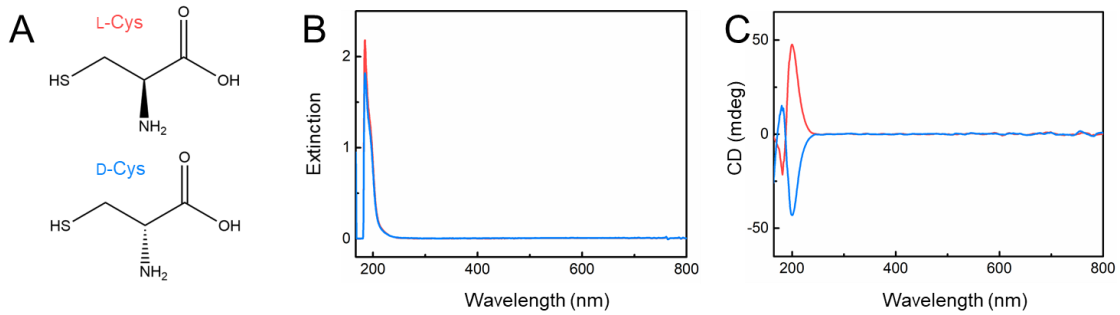


**Figure 2.2** (A) Chemical structures, (B) extinction and (C) CD spectra of L-/D-Cys (5mM).

## Characterization of c-CGS Au NRs

The preparation of c-CGS Au NRs was divided into two steps: the first step was the growth of gold nanobridges as connecting Au NRs to gold shells, and the second step was the growth of gold shells for connecting neighboring nanobridges and encapsulating the adsorbed Cys (**Figure 2.3A**).

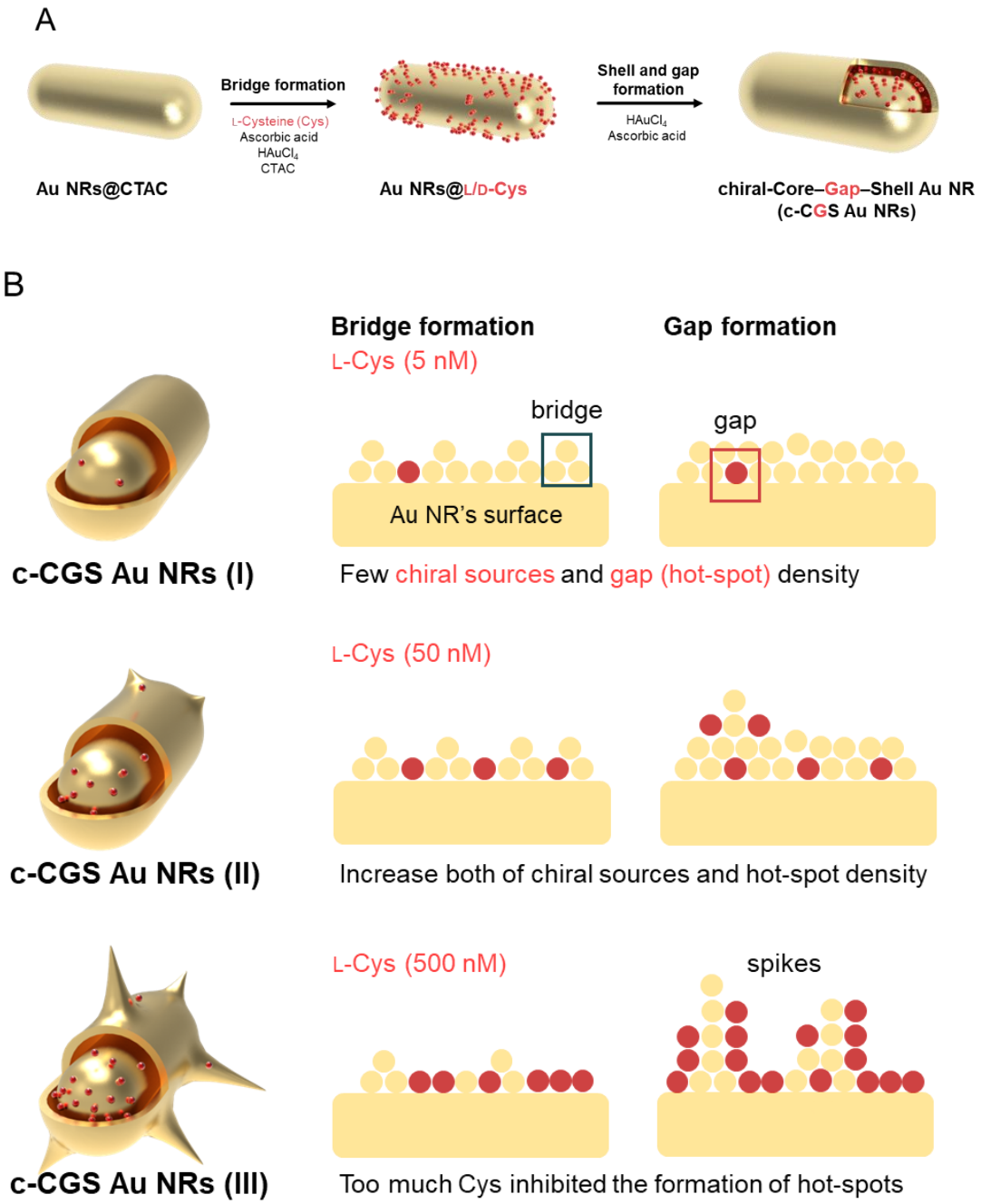


**Figure 2.3** (A) Growth steps and (B) mechanisms of c-CGS Au NRs at different Cys concentrations.

In detail (**Figure 2.3B**), the formation of gold nanobridges relies on the reduction of the first injected lower concentration of gold precursors on the surface of the Au NRs, in conjunction with the competitive adsorption of Cys in the environment. On one hand, due to the strong affinity of thiol groups for the gold surface, Cys readily undergoes ligand exchange with the CTAC molecules on the gold surface. On the other hand, Cys molecules can form thiolate-Au(I) complexes with the gold precursor, thereby reducing the reduction rate.[27] The two mechanisms mentioned above induce the reduction of the gold precursor on the surface of Au NRs, primarily following the Volmer-Weber growth model (island growth).[28] This results in the formation of gold nanobridges and the exposure of fresh sites. It is worth noting that different concentrations of Cys would affect the number of gold nanobridges and fresh sites, consequently affecting the subsequent deposition of gold atoms.

In the second step, a higher concentration of the gold precursor was injected into the solution to initiate the growth of the gold shells. It's important to note that when a lower concentration of Cys (5 nM) was present in the environment, gold atoms uniformly deposited along all faces of the Au NRs, resulting in conformal growth (c-CGS Au NRs (I), length of 142 nm, width of 68 nm, aspect ratio of 2.09), with an increase in both length and width of about 30 nm (**Figure 2.4A**). However, when a moderate concentration of Cys (50 nM) was present, the Au NRs tended to undergo lateral overgrowth (c-CGS Au NRs (II), length of 138 nm, width of 77 nm, aspect ratio of 1.79), and grew a spike in occasional cases, probably because Cys preferentially occupied the ends of the Au NRs (**Figure 2.4B**). With further increases in Cys concentration (500 nM), the island growth mode was amplified, a large number of free strong ligands bonding immediately to freshly exposed crystal faces induced locally anisotropic growth and inhibited the formation of hot-spots. The high-density chiral molecules on the crystal faces may also direct the enantioselective deposition of Au atoms, leading to the appearance of multiple spikes on the surface (c-CGS Au NRs (III), **Figure 2.4C**). In summary, the shell was formed by connecting the adjacent nanobridges and defining the intragap with the core.

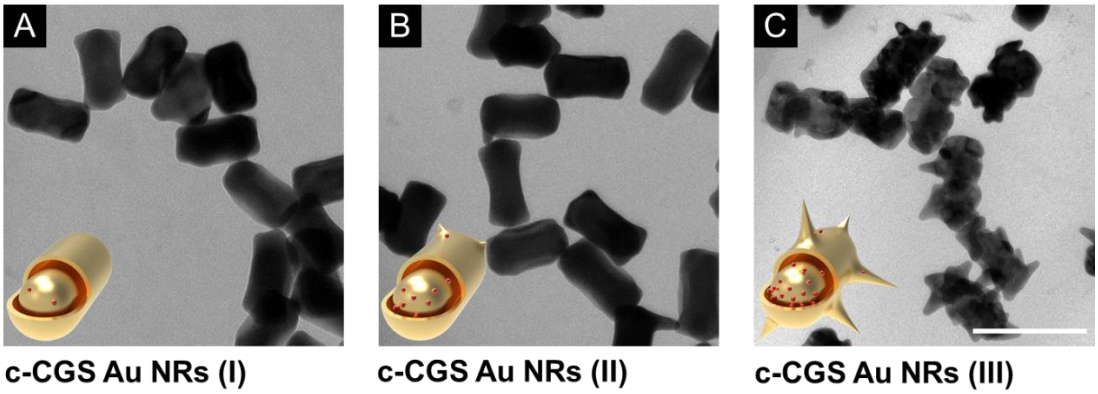


**Figure 2.4**. (A) TEM image and schematic illustration of c-CGS Au NRs (I) prepared using 5 nM of L-Cys. (B) TEM image and schematic illustration of c-CGS Au NRs (II) prepared using 50 nM of L-Cys. (C) TEM image and schematic illustration of c-CGS Au NRs (III) prepared using 500 nM of L-Cys. The scale bars are 200 nm.

By comparing the extinction spectra, it was found that the LSPR properties were related to the Cys concentration but not to the conformation. For example, the L- or D-Cys-induced c-CGS Au NRs (I) and c-CGS Au NRs (II) exhibited redshifts in both the T-LSPR and L-LSPR, which could be attributed to the lateral overgrowth of the NRs and the resonance caused by the formation of intra gaps (**Figure 2.5**). It's worth noting that the change in the aspect ratio of NRs before and after growth is often used as an indicator of the shift in the L-LSPR. However, in this composite structure, the shift in L-LSPR was difficult to assess through a single criterion and required analysis that combined structural changes and plasmon coupling.[29] Similarly, due to the presence of multiple spikes on the surface of c-CGS Au NRs (III), its L-LSPR underwent a significant redshift, similar to that previously reported for gold nanostars.[30]

Interestingly, c-CGS Au NRs obtained after growth induced by L- or D-Cys showed an opposite chiral response, implying a clear correlation of $CD_{LSPR}$ with the conformation of Cys. During shell growth, the low concentration (5 nM) of Cys molecules was unable to support a significant chiral response due to the less quantity of chiral sources and hot-spots (**Figure 2.5 top**), while medium concentration (50 nM) was considered to have the opportunity to increase both of chiral sources and hot-spot

density while maintaining the simple rod shape. It is worth noting that the $CD_{T\text{-}LSPR}$ peak induced by the T-LSPR exhibited a narrow shape with high intensity (**Figure 2.5 middle**). With further increases in Cys concentration (500 nM, 2500 nM and 5000 nM), due to the irregular growth on the NR surface, the $CD_{LSPR}$ peaks became dispersed, and their intensity decreased, making it challenging to predict and understand them through LSPR properties (**Figure 2.5 bottom and Figure 2.6**). This was not an ideal situation for the tailoring and manipulation of the LSPR properties and CD responses as these rely heavily on the morphology of the particles and would become more complicated under the above conditions.

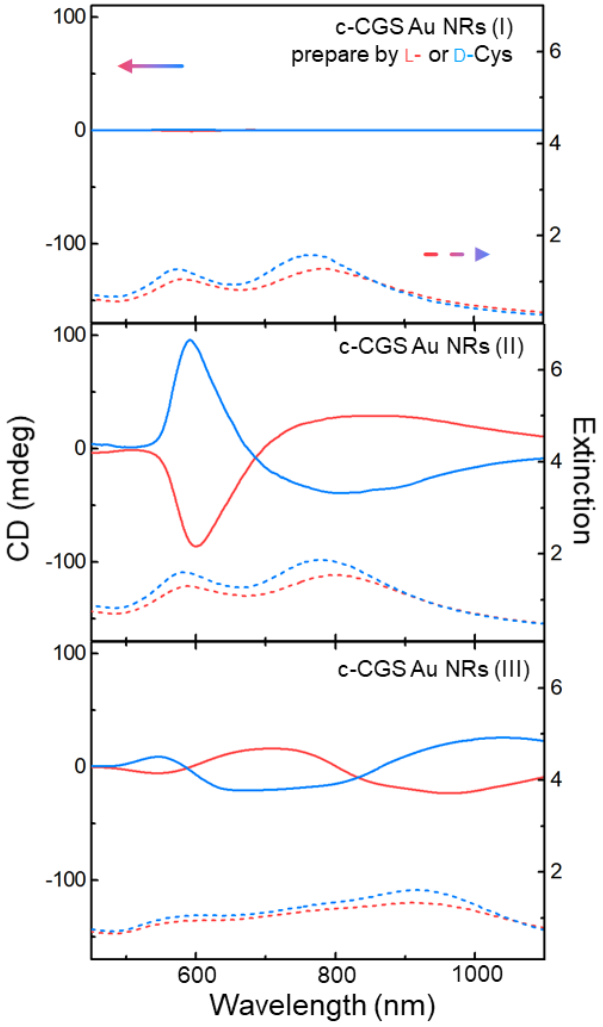


**Figure 2.5** CD (solid curves) and extinction (dashed curves) spectra of c-CGS Au NRs synthesized in the presence of different concentrations of Cys (top 5 nM, middle 50 nM, and bottom 500 nM). Red and blue curves correspond to L-Cys and D-Cys groups, respectively.

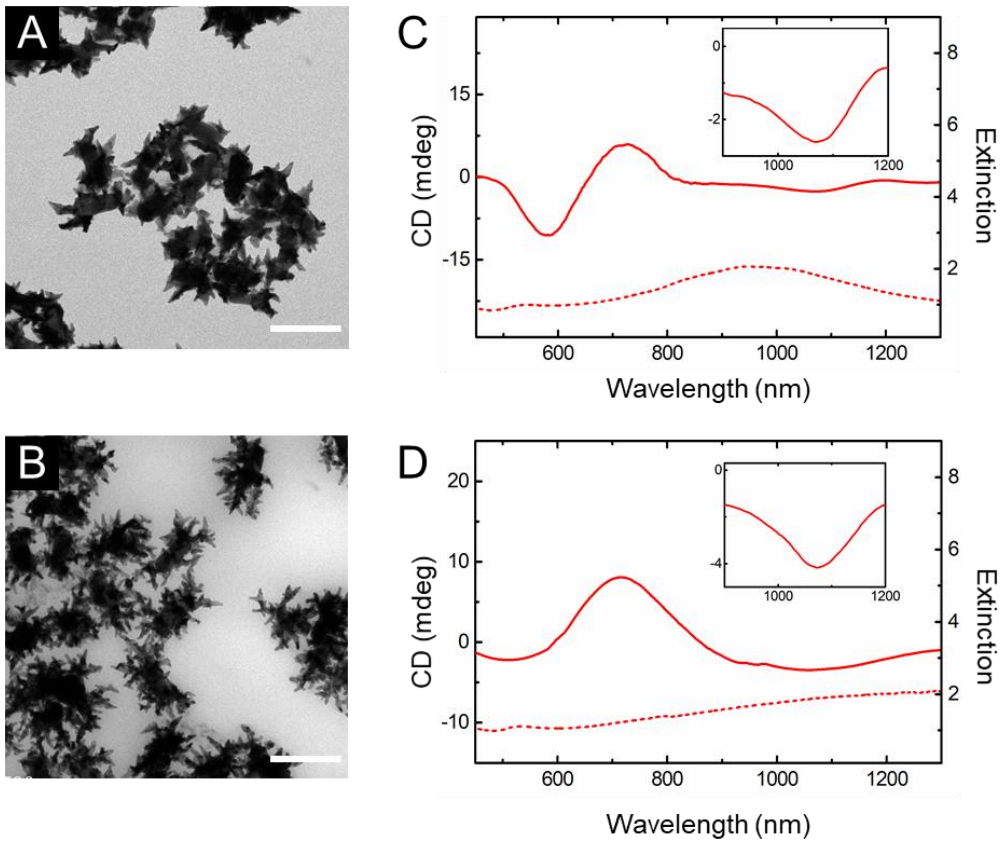


**Figure 2.6** (A) and (B) TEM images of c-CGS Au NRs prepared using 2500/5000 nM of L-Cys, from top to bottom. (C) and (D) CD (solid curves) and extinction (dashed curves) spectra of c-CGS Au NRs synthesized in the presence of 2500/5000 nM of L-Cys, from top to bottom. The inset are local magnification CD spectra. The scale bars are 200 nm.

Through calculations, the concentration of Au NRs was determined to be x mol. Under the condition of complete adsorption of Cys at the highest concentration (500 nM), each Au NR possessed 2530 Cys molecules. Due to the larger curvature of the Au NR end facet [111] and lower spatial hindrance, assuming the above molecules occupied the end facet of the Au NR completely, there was an adsorption of 0.5 Cys/nm$^2$. However, it was reported that the coverage of Cys molecules on the Au [111] surface formed a complete monolayer at a rate of 3.0 Cys/nm$^2$. Consequently, Cys adsorbed on the surface of Au NRs in the form of a sub-monolayer. Therefore, the internal gaps might have exhibited discontinuity, and due to the size of Cys being approximately 0.8 nm, only very small distances could be observed (**Figure 2.7**).

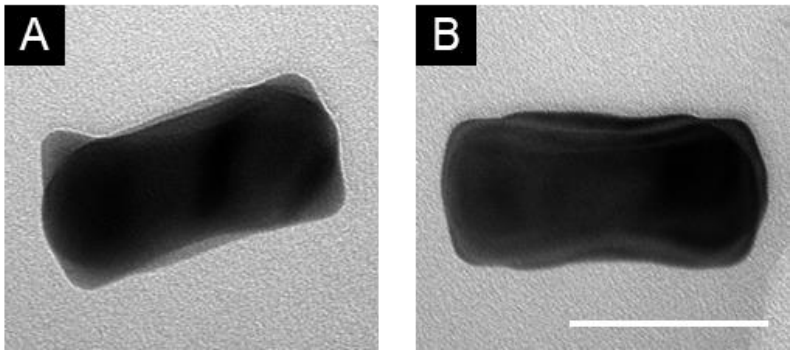


**Figure 2.7** (A) and (B) TEM images of c-CGS Au NRs (II). The scale bar are 100 nm.

Moreover, these c-CGS Au NRs showed greatly enhanced chiral responses compared to the case before shell growth (**Figure 2.8**), and the intensity was almost unchanged after removal of the Cys molecules from the outer surface of the shell (**Figure 2.9**), suggesting that the enhancement effect arose from the natural electromagnetic field hot-spots in the intragap.

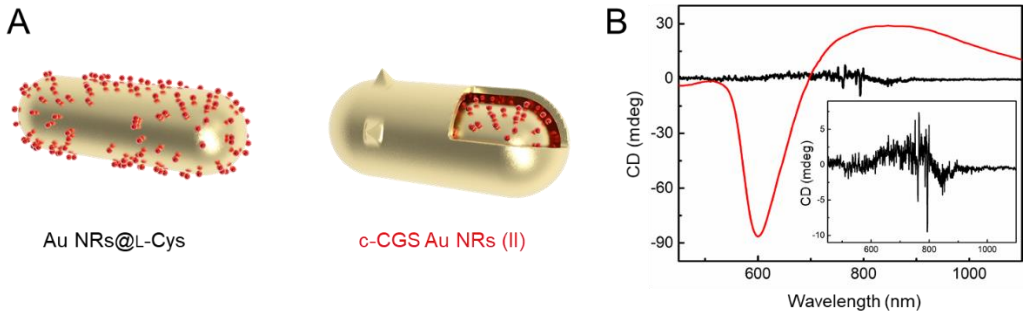


**Figure 2.8** (A) Schematic illustration and (B) CD spectra of Au NRs@L-Cys (black curves) and c-CGS Au NRs (II) (red curve).

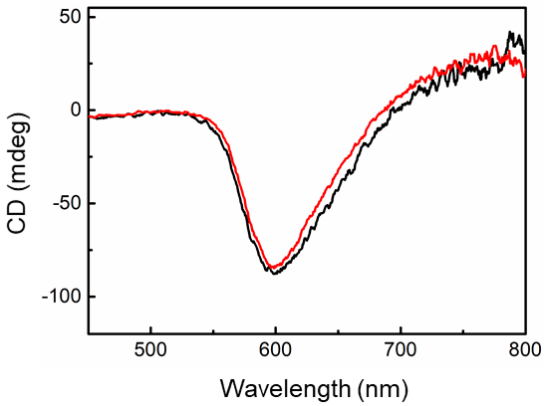


**Figure 2.9** CD spectra of c-CGS Au NRs (II) before (black curve) and after (red curve) treatment with $NaBH_4$.

Notably, Although it is an indisputable fact that the L-LSPR of Au NRs possesses a more prominent advantage in the active plasmonics, the stronger chiral response is a necessary prerequisite to be considered for active chiral plasmonics.[31, 32] The $CD_{T\text{-}LSPR}$ of c-CGS Au NRs (II) showed the strongest chiral intensity, with a *g*-factor about 0.0015 in the absolute value around 600 nm (**Figure 2.10**), implying nonnegligible potential in active chiral plasmon studies.

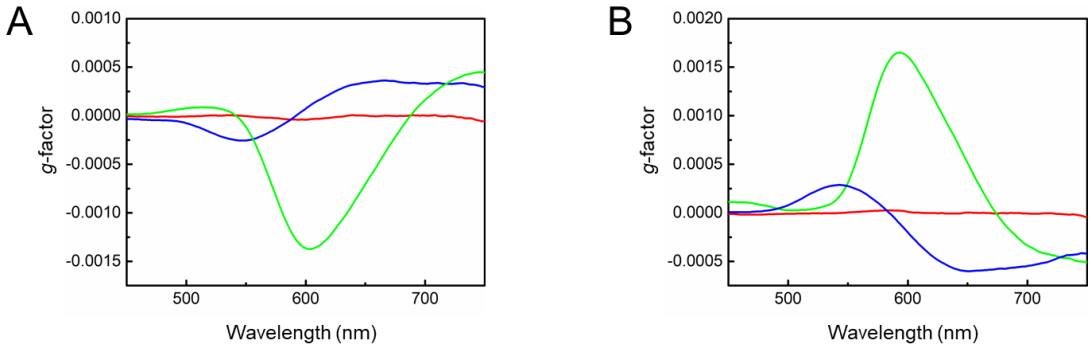


**Figure 2.10** g-factor diagrams of c-CGS Au NRs (I) (red curves), (II) (green curves) and (III) (blue curves) after induction at different concentrations of L-Cys (A) and (B) D-Cys.

## Characterization of Au NSs and c-CGS Au NSs

Furthermore, in consideration of the fact that the LSPR of Au NSs is close to the T-LSPR of Au NRs in terms of the extinction spectrum, similar c-CGS Au NSs were prepared (**Figure 2.11**). Although the c-CGS Au NSs also exhibited an enhancement for the chiral signal compared to the Cys-attached Au NSs, their CD intensity was still very weak and was accompanied by strong background noise (**Figure 2.12**). The reason for this may be their isotropic structure, which provides less potential for symmetry breaking of the internal electron oscillation paths, resulting in lower resonance coefficients, poorer chiral activities, and weaker tunability.[33]

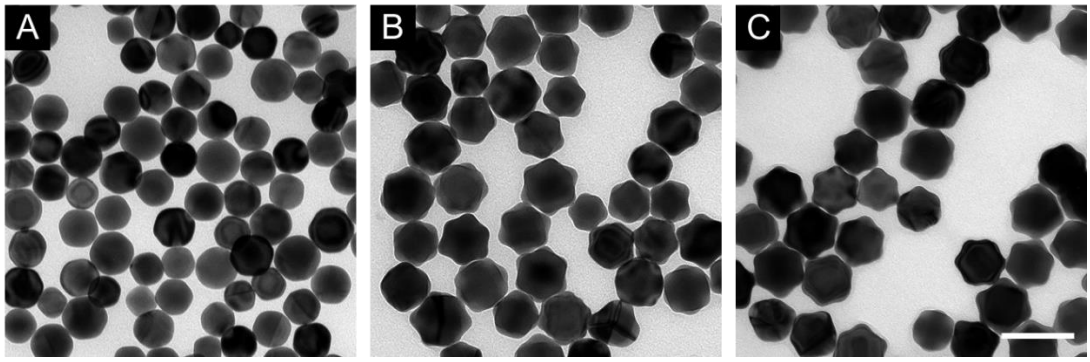


**Figure 2.11** TEM images of (A) Au NPs, (B) c-CGS Au NSs prepared by L-Cys and (C) c-CGS Au NSs prepared by D-Cys. The scale bar are 100 nm.

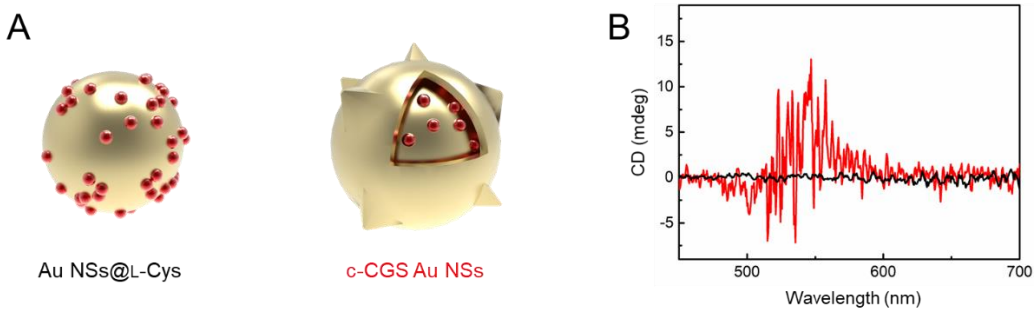


**Figure 2.12** (A) Schematic illustration and (B) CD spectra of Au NSs@L-Cys (black curve) and c-CGS Au NSs (II) (red curve).

## 2.4 Conclusion

The c-CGS Au NRs were prepared by the regrowth of Au NRs as cores, on which different concentrations of L-/D-Cys were adsorbed as a chiral source, providing a gap of sub-monomolecular thickness between the Au core and the shell. The morphology, LSPR properties and $CD_{LSPR}$ response of c-CGS Au NRs prepared from different concentrations of Cys were investigated.

Through control experiments, the enhancement effect has been confirmed to originate from natural electromagnetic hot-spots within the gaps. It is interesting that, although the prominent advantage of L-LSPR in Au NRs within active plasmonics is an undeniable fact, the corresponding induced plasmonic chiroptical properties exhibit a contrasting phenomenon. For instance, c-CGS Au NRs (II) prepared with a moderate concentration of Cys (50 nM) displayed the strongest $CD_{T\text{-}LSPR}$ response, with a g-factor value of 0.0015 (at a wavelength of 600 nm). This implies significant potential in the study of active chiral plasmonics.

## 2.5 References


[1] Nesterov, M. L.; Yin, X.; Schäferling, M.; Giessen, H.; Weiss, T. The Role of Plasmon-Generated Near Fields for Enhanced Circular Dichroism Spectroscopy. *ACS Photonics* **2016**, *3*, 578-583.

[2] Chulhai, D. V.; Jensen, L. Plasmonic Circular Dichroism of 310- and α-Helix Using a Discrete Interaction Model/Quantum Mechanics Method. *J. Phys. Chem. A* **2014**, *119*, 5218-5223.

[3] Ben-Moshe, A.; Maoz, B. M.; Govorov, A. O.; Markovich, G. Chirality and Chiroptical Effects in Inorganic Nanocrystal Systems with Plasmon and Exciton Resonances. *Chem. Soc. Rev.* **2013**, *42*, 7028-7041.

[4] Ma, W.; Kuang, H.; Xu, L.; Ding, L.; Xu, C.; Wang, L.; Kotov, N. A. Attomolar DNA Detection with Chiral Nanorod Assemblies. *Nat. Commun.* **2013**, *4*, 2689.

[5] Wu, X.; Xu, L.; Liu, L.; Ma, W.; Yin, H.; Kuang, H.; Wang, L.; Xu, C.; Kotov, N. A. Unexpected Chirality of Nanoparticle Dimers and Ultrasensitive Chiroplasmonic Bioanalysis. *J. Am. Chem. Soc.* **2013**, *135*, 18629-18636.

[6] Zheng, G.; He, J.; Kumar, V.; Wang, S.; Pastoriza-Santos, I.; Pérez-Juste, J.; Liz-Marzán, L. M.; Wong, K.-Y. Discrete Metal Nanoparticles with Plasmonic Chirality. *Chem. Soc. Rev.* **2021**, *50*, 3738-3754.

[7] Urban, M. J.; Shen, C.; Kong, X.-T.; Zhu, C.; Govorov, A. O.; Wang, Q.; Hentschel, M.; Liu, N. Chiral Plasmonic Nanostructures Enabled by Bottom-Up Approaches. *Annu. Rev. Phys. Chem.* **2019**, *70*, 275-299.

[8] Ma, W.; Xu, L.; de Moura, A. F.; Wu, X.; Kuang, H.; Xu, C.; Kotov, N. A. Chiral Inorganic Nanostructures. *Chem. Rev.* **2017**, *117*, 8041-8093.

[9] Liu, Z.; Ai, J.; Kumar, P.; You, E.; Zhou, X.; Liu, X.; Tian, Z.; Bouř, P.; Duan, Y.; Han, L.; Kotov, N. A.; Ding, S.; Che, S. Enantiomeric Discrimination by Surface-Enhanced Raman Scattering–Chiral Anisotropy of Chiral Nanostructured Gold Films. *Angew. Chem. Int. Ed.* **2020**, *59*, 15226.

[10] Lu, J.; Xue, Y.; Bernardino, K.; Zhang, N-N.; Gomes, W. R.; Ramesar, N. S.; Liu, S.; Hu, Z.; Sun, T.; Moura, A. F. D.; Kotov. N. A.; Liu, K. Enhanced Optical Asymmetry in Supramolecular Chiroplasmonic Assemblies with Long-Range Order. *Science* **2021**, *371*,1368-1374.

[11] Negrín-Montecelo, Y.; Movsesyan, A.; Gao, J.; Burger, S.; Wang, Z. M.; Nlate, S.; Pouget, E.; Oda, R.; Comesaña-Hermo, M., Govorov, A. O.; Correa-Duarte, M. A. Chiral Generation of Hot Carriers for Polarization-Sensitive Plasmonic Photocatalysis. *J. Am. Chem. Soc.* **2022**, *144*, 1663-1671.

[12] Miandashti, A. R.; Khorashad, K. L.; Kordesch, M. E.; Govorov, A. O.; Richardson, H. H. Experimental and Theoretical Observation of Photothermal Chirality in Gold Nanoparticle Helicoids. *ACS Nano* **2020**, *14*, 4188-4195.

[13] Govorov, A. O.; Fan, Z.; Hernandez, P.; Slocik, J. M.; Naik, R. R. Theory of Circular Dichroism of Nanomaterials Comprising Chiral Molecules and Nanocrystals: Plasmon Enhancement, Dipole Interactions, and Dielectric Effects. *Nano Lett.* **2010**, *10*, 1374-1382.

[14] Zhang, H.; Govorov, A. O. Giant Circular Dichroism of a Molecule in a Region of Strong Plasmon Resonances Between Two Neighboring Gold Nanocrystals. *Phys. Rev. B*, **2013**, *87*, 075410.

[15] Langer, J.; de Aberasturi, D.J.; Aizpurua, J.; Alvarez-Puebla, R. A.; Auguie, B.; Baumberg, J. J.; Bazan, G. C.; Bell, S. E. J.; Boisen, A.; Brolo, A. G.; Choo, J.; Cialla-May, D.; Deckert, V.; Fabris, L.; Faulds, K.; de Abajo, F. J. G.; Goodacre, R.; Graham, D.; Haes, A. J.; Haynes, C. L.; Huck, C.; Itoh, T.; Ka, M.; Kneipp, J.; Kotov, N. A.; Kuang, H.; Le Ru, E. C.; Lee, H. K.; Li, J. F.; Ling, X. Y.; Maier, S. A.; Mayerhofer, T.; Moskovits, M.; Murakoshi, K.; Nam, J. M.; Nie, S.; Ozaki, Y.; Pastoriza-Santos, I.; Perez-Juste, J.; Popp, J.; Pucci, A.; Reich, S.; Ren, B.; Schatz, G. C.; Shegai, T.; Schlucker, S.; Tay, L. L.; Thomas, K. G.; Tian, Z.-Q.; Van Duyne, R. P.; Vo-Dinh, T.; Wang, Y.; Willets, K. A.; Xu, C.; Xu, H.; Xu, Y.; Yamamoto, Y. S.; Zhao, B.; Liz-Marzan, L. M. Present and Future of Surface-Enhanced Raman Scattering. *ACS Nano* **2020**, *14*, 28-117.

[16] Mitomo, H.; Horie, K.; Matsuo, Y.; Niikura, K.; Tani, T.; Naya, M; Ijiro, K. Active Gap SERS for the Sensitive Detection of Biomacromolecules with Plasmonic Nanostructures on Hydrogels. *Adv. Opt. Mater.* **2015**, *4*, 259-263.

[17] Govorov, A. O. Plasmon-Induced Circular Dichroism of a Chiral Molecule in the Vicinity of Metal Nanocrystals. Application to Various Geometries. *J. Phys. Chem. C* **2011**, *115*, 7914-7923.

[18] Zhu, Z.; Liu, W.; Li, Z.; Han, B.; Zhou, Y.; Gao, Y.; Tang, Z. Manipulation of Collective Optical Activity in One-Dimensional Plasmonic Assembly. *ACS Nano* **2012**, *6*, 2326-2332.

[19] Han, B.; Zhu, Z.; Li, Z.; Zhang, W.; Tang, Z. Conformation Modulated Optical Activity Enhancement in Chiral Cysteine and Au Nanorod Assemblies. *J. Am. Chem. Soc.* **2014**, *136*, 16104-16107.

[20] Kneer, L. M.; Roller, E. M.; Besteiro, L. V.; Schreiber, R.; Govorov, A. O.; Liedl, T. Circular Dichroism of Chiral Molecules in DNA-Assembled Plasmonic Hotspots. *ACS Nano* **2018**, *12*, 9110-9115.

[21] Kim, J.-M.; Lee, C.; Lee, Y.; Lee, J.; Park, S.-J.; Park, S.; Nam, J.-M. Synthesis,

Assembly, Optical Properties, and Sensing Applications of Plasmonic Gap Nanostructures. *Adv. Mater.* **2021**, *33*, 2006966.

[22] Wu, X.; Xu, L.; Ma, W.; Liu, L.; Kuang, H.; Yan, W.; Wang, L.; Xu, C. Gold Core-DNA-Silver Shell Nanoparticles with Intense Plasmonic Chiroptical Activities. *Adv. Funct. Mater.* **2015**, *25*, 850-854.

[23] Hao, C.; Xu, L.; Ma, W.; Wu, X.; Wang, L.; Kuang, H.; Xu, C. Unusual Circularly Polarized Photocatalytic Activity in Nanogapped Gold–Silver Chiroplasmonic Nanostructures. *Adv. Funct. Mater.* **2015**, *25*, 5816-5822.

[24] Hanske, C.; González-Rubio, G.; Hamon, C.; Formentín, P.; Modin, E.; Chuvilin, A.; Guerrero-Martínez, A.; Marsal, L. F.; Liz-Marzán, L. M. Large-Scale Plasmonic Pyramidal Supercrystals via Templated Self-Assembly of Monodisperse Gold Nanospheres. *J. Phys. Chem. C* **2017**, *121*, 10899-10906.

[25] Ni, W.; Kou, X.; Yang, Z.; Wang, J. Tailoring Longitudinal Surface Plasmon Wavelengths, Scattering and Absorption Cross Sections of Gold Nanorods. *ACS Nano* **2008**, *2*, 677-686.

[26] Yan, J.; Feng, W.; Kim, J.-Y.; Lu, J.; Kumar, P.; Mu, Z.; Wu, X.; Mao, X.; Kotov, N. A. Self-Assembly of Chiral Nanoparticles into Semiconductor Helices with Tunable near-Infrared Optical Activity. *Chem. Mater.* **2019**, *32*, 476-488.

[27] Lee, H.-E.; Yang, K. D.; Yoon, S. M.; Ahn, H.-Y.; Lee, Y. Y.; Chang, H.; Jeong, D. H.; Lee, Y.-S.; Kim, M. Y.; Nam, K. T. Concave Rhombic Dodecahedral Au Nanocatalyst with Multiple High-Index Facets for $CO_2$ Reduction. *ACS Nano* **2015**, *9*, 8384-8393.

[28] Wang, G.; Liu, Y.; Gao, C.; Guo, L.; Chi, M.; Ijiro, K.; Maeda, M.; Yin, Y. Island Growth in the Seed-Mediated Overgrowth of Monometallic Colloidal Nanostructures. *Chem* **2017**, *3*, 678-690.

[29] Hong, S.; Acapulcoaaa, J. A. I.; Jang, H. Y.; Park, S. Au Nanodisk-Core Multishell Nanoparticles: Synthetic Method for Controlling Number of Shells and Intershell Distance. *Chem. Mater.* **2014**, *26*, 3618-3623.

[30] Kuttner, C.; Piotto, V.; Liz-Marzán, L. M. Plasmonic Gradient Arrays for Rapid Screening of Surface-Enhanced Raman Scattering Efficiency: Particle Libraries of Gold Nanostars. *Chem. Mater.* **2021**, *33*, 8904-8914.

[31] González-Rubio, G.; Mosquera, J.; Kumar, V.; Pedrazo-Tardajos, A.; Llombart, P.; Solís, D. M.; Lobato, I.; Noya, E. G.; Guerrero-Martínez, A.; Taboada, J. M.; Obelleiro, F.; MacDowell, L. G.; Bals, S.; Liz-Marzán, L. M. Micelle-Directed Chiral Seeded Growth on Anisotropic Gold Nanocrystals. *Science* **2020**, *368*, 1472-1477.

[32] Lee, H.-E.; Ahn, H.-Y.; Mun, J.; Lee, Y. Y.; Kim, M.; Cho, N. H.; Chang, K.; Kim, W. S.; Rho, J.; Nam, K. T. Amino-Acid- and Peptide-Directed Synthesis of Chiral Plasmonic Gold Nanoparticles. *Nature* **2018**, *556*, 360-365.

[33] Kong, X. T.; Besteiro, L. V.; Wang, Z.; Govorov, A. O. Plasmonic Chirality and Circular Dichroism in Bioassembled and Nonbiological Systems: Theoretical Background and Recent Progress. *Adv. Mater.* **2018**, *32*, 1801790.

# *Chapter 3*

## *Dynamic Tuning of Plasmonic Chiroptical Properties by Stimulation of the Dielectric Active Layer*

## 3.1 Introduction

In principle, the chirality of a substance is a static and well-defined property.[1] However, $CD_{LSPR}$, a novel optical response that is active in the visible and near-infrared regions, depending on the molecular conformation and the LSPR properties of the nanoparticles, has attracted great interest in the field of chiral plasmonics with regard to the customization and dynamic tuning of chiroptical activities, such as signal intensity changes or response reversals, as well as wavelength shifts.[2] To date, most studies on reconfigurable active chiral plasmonic nanostructures have focused on dimeric or three-dimensional assemblies.[3-7] For example, the artificial tuning or inversion of CD responses was achieved by the appropriate modulation of the chiral templates (e.g., DNA origami, cellulose liquid crystals, etc.) or manipulation of the behavior of nanoparticle assembly/disassembly with the assistance of external stimuli.[8-16] However, there have been very few reports on the dynamically tunable plasmonic chiroptical activities of discrete metal nanoparticles, especially in wavelength shifts, mainly due to the vulnerability of most chiral molecules to external stimuli and the instability of the nanoparticles and their unadjustable $\lambda_{LSPR}$.[17, 18]

Except for assembly/disassembly strategies, it is generally difficult to actively and reversibly tune the $\lambda_{LSPR}$ of plasmonic nanoparticles with a specific composition, shape, and size.[19] The $\lambda_{LSPR}$ of simple spherical or rod-shaped particles is as follows[17]

$$\lambda_{LSPR} = \lambda_P(2\varepsilon_m + 1)^{-1/2}$$

where $\lambda_P$ is the wavelength corresponding to the plasma frequency and $\varepsilon_m$ is the environment dielectric constant to influence the LSPR peak position of the particle. Obviously, the variable dielectric material makes discrete active plasmonics possible. Polyaniline (PANI), as an easily fabricated and inexpensive variable dielectric material, has received a good deal of attention due to its excellent stability, fascinating redox chemistry, and doping/de-doping properties.[20] Recently, its stability in water

has been greatly improved by doping with anionic surfactants, which has led to many studies on the tunable plasmonic properties of PANI with gold nanocrystals.[21-25] Interestingly, based on the mechanism of plasmon-induced chirality generation, it makes reasonable to achieve tunable chiral shifting activities with the assistance of the tunable $\lambda_{LSPR}$.

In this chapter, the active dielectric layer PANI was coated on the Au shell surface to provide a reconfigurable dielectric environment for the whole system (c-CGS Au NRs@PANI), leading to the tunable LSPR and resulting in $CD_{LSPR}$ optical activities within the visible region in response to the external pH and electric potential modulation. Satisfyingly, c-CGS Au NRs@PANI exhibited a wide wavelength range of $CD_{LSPR}$ modulation (around 60 nm shift), stability (more than 100 cycles), accuracy (10 nm/V), and fast switching response (<1 s), further enhancing their potential in fields such as chiral optical device fabrication.

## 3.2 Experimental Section

### Materials

Sodium dodecyl sulfate (SDS, ACS, ≥99.0%), aniline (ACS, ≥99.0%), ammonium persulfate (AR, ≥98%), anhydrous ethanol, sodium hydroxide (97%, sheet-like) and sodium chloride (GR, 99.5%) were purchased from Aladdin. *n*-hexane (GR) was obtained from Sinopharm Chemical Reagent Co., Ltd. (Shanghai). ITO conductive glass (square resistance is 6 Ω, indium tin oxide layer thickness is 185 nm) was purchased from South China Xiangcheng Science and Technology Co., Ltd.

### Characterization

Electrochemical measurements were performed on a CHI 760E electrochemical workstation (Chenhua Instrument Company, Shanghai, China). A conventional three-electrode system was adopted, using an ITO conductive glass as a working electrode, a platinum wire as a counter electrode and an Ag/AgCl (3 M KCl) electrode as a reference electrode. Other instruments used in this chapter are listed in chapter 2.

### Preparation of c-CGS Au NRs@PANI

The coating of Au NRs or Au NSs with PANI was realized by surfactant-assisted chemical oxidative polymerization. For example, as-synthesized c-CGS Au NRs (II) (1.5 mL) were centrifuged, and the precipitate was redispersed in a mixture of aniline (25 μL, 44 mM) and SDS (37.5 μL, 40 mM) and shaken vigorously for 1 min. Subsequently, the above solution was mixed with an acidic $(NH_4)_2S_2O_8$ solution (200 μL, 2 mM, in 10 mM HCl) and further shaken for 1 min. Finally, it was let stand undisturbed overnight to obtain the c-CGS Au NRs@PANI.

To remove free PANI after the polymerization process, the supernatant was removed by centrifugation (2936*g*, 10 min) and the precipitate was redispersed in SDS solution (1 mL, 5 mM). The PANI coating of the Au NSs followed the same procedure as that for the Au NRs.

### Fabrication and Transfer of c-CGS Au NRs@PANI Monolayers

The c-CGS Au NRs@PANI monolayer film was prepared at the water–oil liquid-liquid interface. Briefly, c-CGS Au NRs@PANI solution (7 mL) and deionized

water (3 mL) were added to a clean glass culture dish (diameter: 6 cm) and mixed well; then, hexane solution (10 mL) was slowly added to the surface of the above solution to form an immiscible water–oil interface. The anhydrous ethanol (10 mL) was injected into the aqueous phase solution at a uniform rate (0.8 mL/min) via a mechanical syringe pump. This strategy enabled the nanoparticles in the aqueous phase to gradually transfer to the water–oil interface and self-assemble into a monolayer film. After the injection, the culture dish was covered with a glass sheet to control the slow evaporation of the hexane until the film was completely exposed to the water–air interface. Subsequently, an ITO electrode was touched to the monolayer film surface at a specific inclination angle so that the film was smoothly transferred to the ITO surface by capillary forces. After immersion in water overnight to remove excess SDS, the film was then transferred to an HCl solution (0.1 M) for 1 h to ensure that the PANI was completely converted to an ES state.

## Dual Response of c-CGS Au NRs@PANI for Plasmonic and Chiral Spectroscopic Properties

The pH stimulation of LSPR and the chiral spectroscopic properties of c-CGS Au NRs@PANI were realized with HCl (0.1 M) and NaOH (0.1 M). To ensure the complete doping/de-doping of the internal protons of PANI, oscillation for 30 s was necessary before spectroscopic measurements. In order to achieve the gentle transitions between ES, LB, and PB states and to avoid electrochemical degradation of the PANI layer, damage to the ITO substrate, and potential hydrogen evolution reactions, the HCl solution (0.01 M) with NaCl (0.5 M) was used as the electrolyte and the voltage window was limited to 0.4 to −0.3 V. UV–vis and CD spectra were recorded simultaneously after pH and electric potential stimulation. Cyclic voltammetric measurements were performed at a scan rate of 0.1 V/s. To better compare the LSPR shift responses, all normalized spectra and the CD spectra were converted from T-LSPR intensity to a value of 1.

## 3.3 Results and Discussion

### Optimization of PANI Dielectric Layer Thickness

The coating of PANI on the surface of c-CGS Au NRs was achieved through surfactant-assisted chemical oxidative polymerization (**Figure 3.1A**).[21] In this process, aniline was initially embedded within micelles formed by the anionic surfactant SDS. Subsequently, these micelles adsorbed onto the CTAC bilayers on the surface of NRs through electrostatic interactions. Upon the addition of the oxidizing agent $(NH_4)_2S_2O_8$, aniline underwent polymerization on the gold surface and in the solution to form the emeraldine salt form of PANI. Finally, c-CGS Au NRs@PANI and free PANI polymer were separated through centrifugation. Additionally, the thickness of the PANI layer can be adjusted by changing the aniline monomer concentration, controlling the polymerization time, or repeating the coating process multiple times. In this project, the L-Cys-induced c-CGS Au NRs (II)@PANI [L-c-CGS Au NRs (II)@PANI] with a layer thickness of 7, 11, or 14 nm were obtained by repeating the polymerization cycles (**Figure 3.1B-D**).

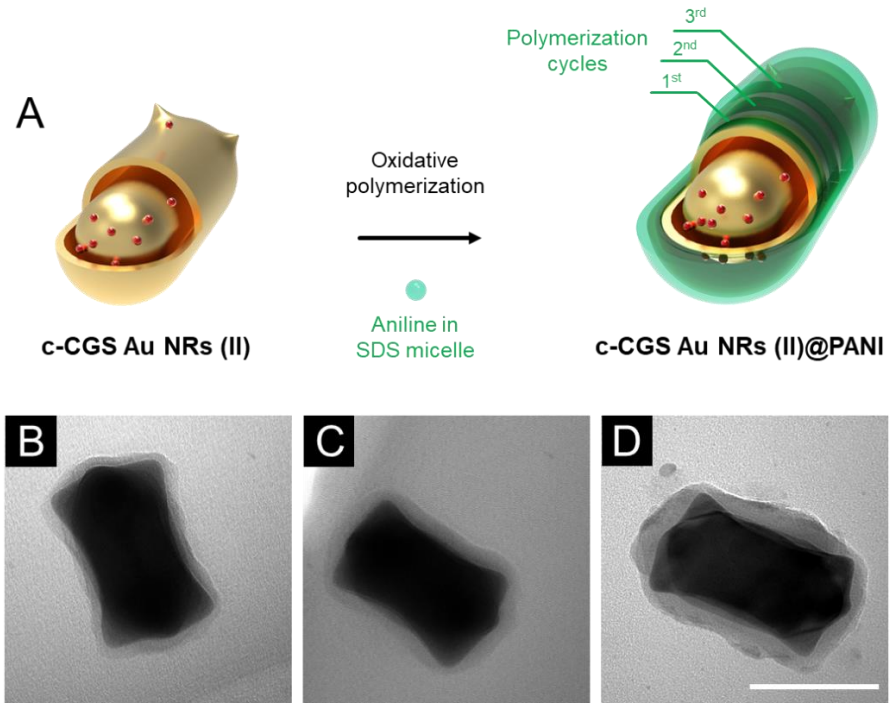


**Figure 3.1** (A) Schematic illustration for coating c-CGS Au NRs (II) with a PANI layer. TEM images of L-c-CGS Au NRs (II)@PANI after (B) one, (C) two, and (D) three cycles. The scale bars are 100 nm.

In previous discrete active plasmonic systems, the LSPR shifts of the plasmonic nanoparticles always followed the relationship shown below[17]

$$\Delta\lambda_{shift} = m\Delta n(1 - e^{-2d/l_d})$$

where $m$ is the refractive index sensitivity of the plasmonic nanoparticle, $\Delta n$ is the variation of the refractive index between different dielectric environments, $d$ is the effective thickness of the dielectric environment, and $l_d$ is the decay length of the electromagnetic field on the plasmonic nanoparticle surface. Obviously, the $\Delta\lambda_{shift}$ is strongly related to the $d$ and $\Delta n$ values.

Firstly, $d$ was defined by the thickness of the outermost dielectric layer, PANI. Due to its refractive index being slightly greater than that of water ($n_{H_2O} \approx 1.33$), an increase in its thickness induced a redshift in the T-LSPR position. However, it was crucial to note that this trend occurred only within the effective thickness range. From the results of T-LSPR redshift (**Figure 3.2**), when the thickness of PANI increased from 11 nm to 14 nm, the redshift had already begun to exhibit a saturation tendency, indicating proximity to the effective thickness of PANI. Additionally, for reference, this redshift behavior was similarly validated on c-CGS Au NSs coated with a layer of PANI (**Figure 3.3**). The appearance of a new peak in the near-infrared region was attributed to the absorption of PANI.

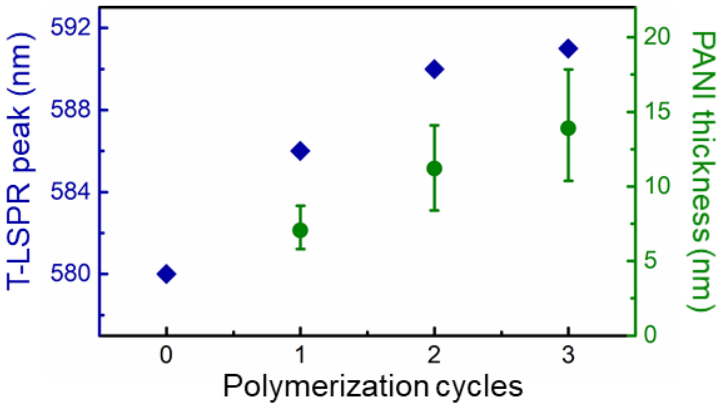


**Figure 3.2** T-LSPR peak positions at pH 2 and PANI layer thickness versus the number of polymerization cycles.

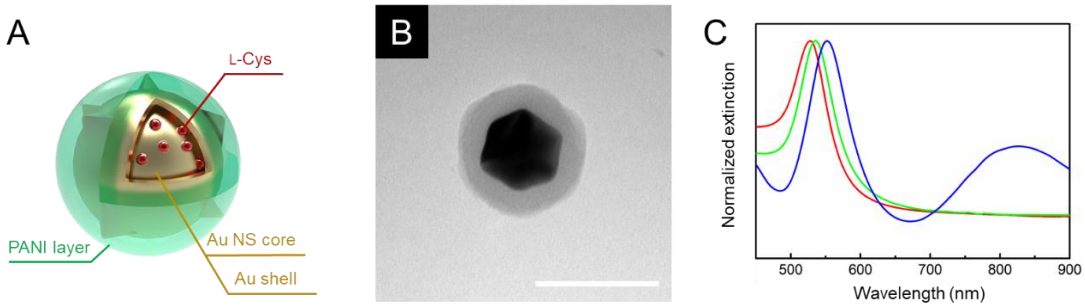


**Figure 3.3** (A) Schematic illustration and (B) TEM image of c-CGS Au NSs@PANI. (C) Normalized extinction spectra of Au NSs (red curve), c-CGS Au NSs (green curve) and c-CGS Au NSs@PANI (blue curve). The scale bar is 100 nm.

Secondly, $\Delta n$ was considered to be provided by the change in refractive index when PANI underwent a chemical transformation. It is well known that PANI can exist in six states with different refractive indices at various pH values and redox states: leucoemeraldine base (LB), leucoemeraldine salt (LS), emeraldine base (EB), emeraldine salt (ES), pernigraniline base (PB), and pernigraniline salt (PS) (**Figure 3.4**).[26] The conditions or means to accomplish the full state transformation are often severe, such as strong acidic environments, changes in aqueous and non-aqueous electrolyte environments, and higher potentials, which will directly affect the lifetime of the materials. In contrast, ES, PB and LB can be transformed in a relatively gentle manner.[23] Correspondingly, the refractive indices of ES ($n_{ES} \approx 1.40$), PB ($n_{PB} \approx 2.05$), and LB ($n_{LB} \approx 1.68$) have been measured in previous reports.[23]

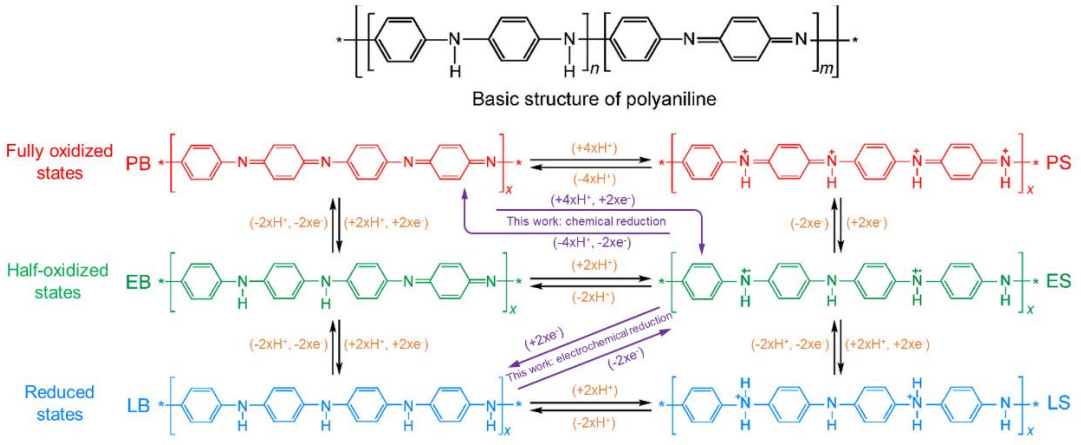


**Figure 3.4** All six different states of PANI and their interconversion.

To understand their LSPR characteristics, the pure PANI solutions (**Figure 3.5A and B top**) and L-c-CGS Au NRs (II)@PANI (**Figure 3.5A and B bottom**) were observed at both pH 2 and pH 12. At pH 2, the T-LSPR (590 nm) and L-LSPR (797 nm) could be easily distinguished, and the ES state itself presented an extinction peak at 875 nm. At pH 12, the ES state was converted into the PB state (556 nm) due to the de-doping of protons, and the proximity of PB and T-LSPR led them to be coupled into a broad peak (646 nm). The red shift of the L-LSPR (from 797 to 863 nm) was also evidenced by the change from the ES to the PB state.

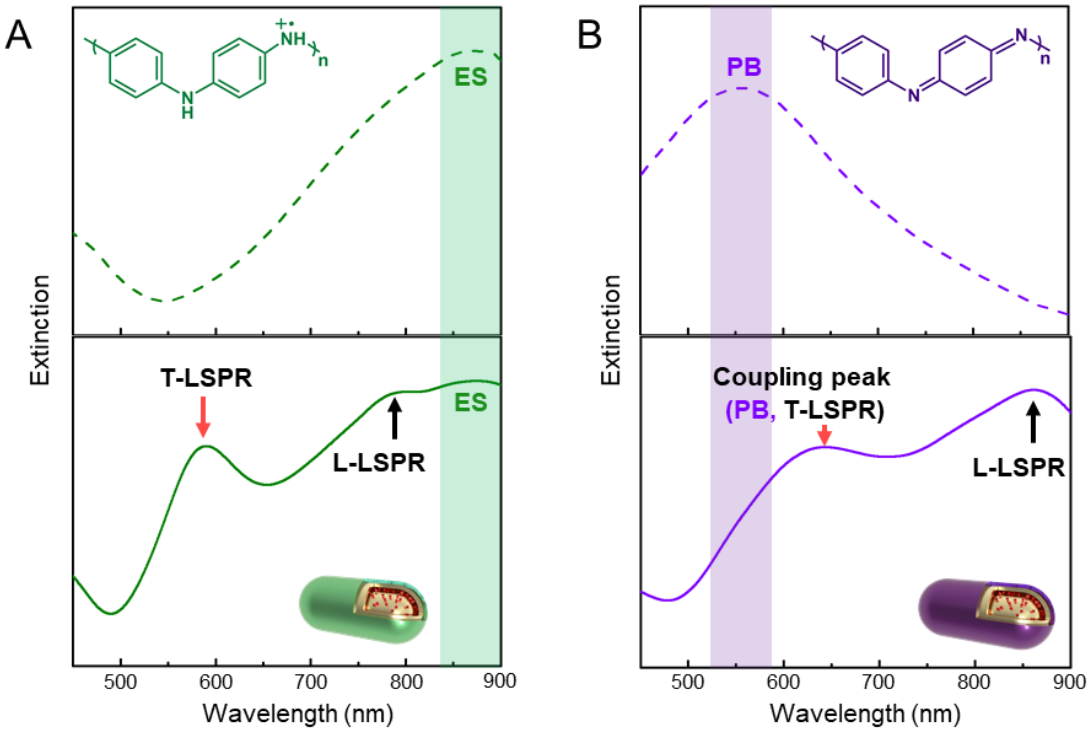


**Figure 3.5** (A) Extinction spectra of pure PANI (dashed curves, top) and L-c-CGS Au NRs (II) coated with an 11 nm-thick PANI layer (solid curves, bottom) at pH 2. (B) Extinction spectra of pure PANI (dashed curves, top) and L-c-CGS Au NRs (II) coated with an 11 nm-thick PANI layer (solid curves, bottom) at pH 12.

A similar phenomenon was observed during the transition between the ES and PB states in c-CGS Au NSs@PANI (**Figure 3.6**). It is noteworthy that, at pH 12, the LSPR peak of nanospheres also engaged in coupling with the PB peak due to their closely proximity.


**Figure 3.6** (A) Schematic illustrations and (B) normalized extinction spectra of the conversion between c-CGS Au NSs@PANI$_{(ES)}$ and c-CGS Au NSs@PANI$_{(PB)}$. (C) Schematic illustrations and (D) normalized extinction spectra of the conversion between c-CGS Au NSs@PANI$_{(ES)}$ and c-CGS Au NSs@PANI$_{(PB)}$.

It should be noted that the PANI layer thickness was important in terms of the following two points. The first point is the need to maximize the shift qualities of the LSPR peaks ($\Delta\lambda_{shift}$) and the potential CD$_{LSPR}$ peak wavelength.

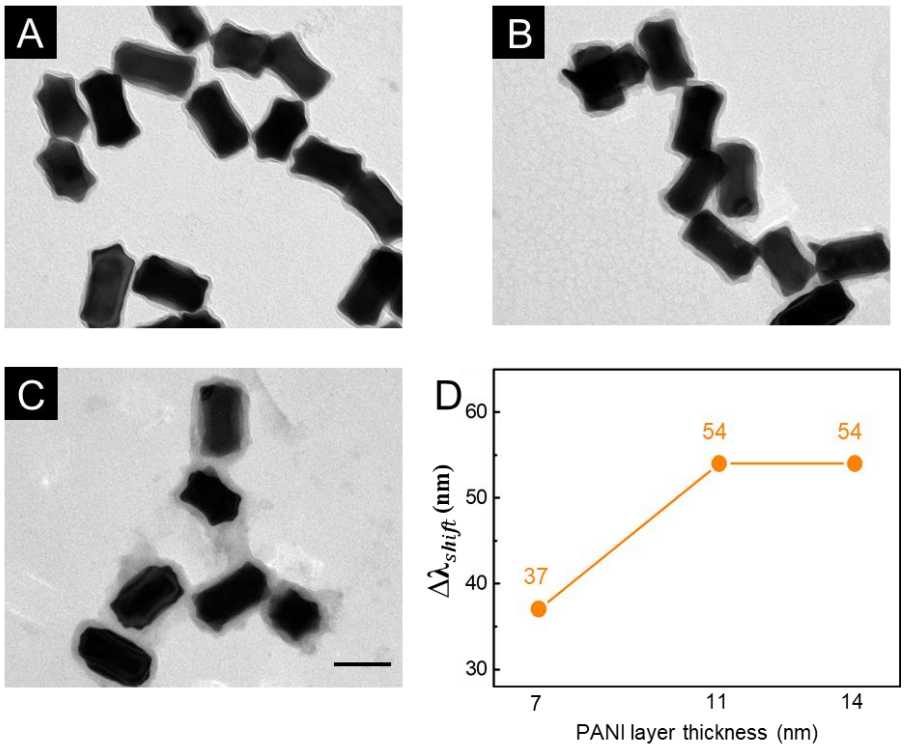


**Figure 3.7** TEM images of L-c-CGS Au NRs (II)@PANI with thicknesses of 7 nm (A), 11 nm (B) and 14 nm (C). (D) The redshifts value in the T-LSPR peaks versus PANI thickness. The scale bars are 100 nm.

Herein, the shift values of the T-LSPR before and after pH conversion were used as a reference indicator to optimize the thickness of the PANI layer, allowing for a comparison of the shift gains conferred by three different thicknesses (**Figure 3.7A-C**). The $\Delta\lambda_{shift}$ of the composite structure with a PANI layer of 11 and 14 nm was the same, both were 54 nm (**Figure 3.7D**).

The second point is the need to avoid excessive loss of chiral response. The reason might be that the achiral PANI shells increasing the total absorption but having little effect on the absorption of LCP or RCP light, resulting in a decrease in the *g*-factor of the asymmetry parameter for c-CGS Au NRs (II) after coating (**Figure 3.8A, B**). Additionally, a very low specific value for the *g*-factor was observed for the composite structure with the Au NSs as the core (**Figure 3.8C, D**), also indicating that anisotropic nanostructures are more suitable for active chiral plasmons. Based on the above considerations, the ideal situation is to obtain a larger peak shift by application of a thinner PANI layer, while avoiding the possible loss of CD signal intensity in response to external stimuli.

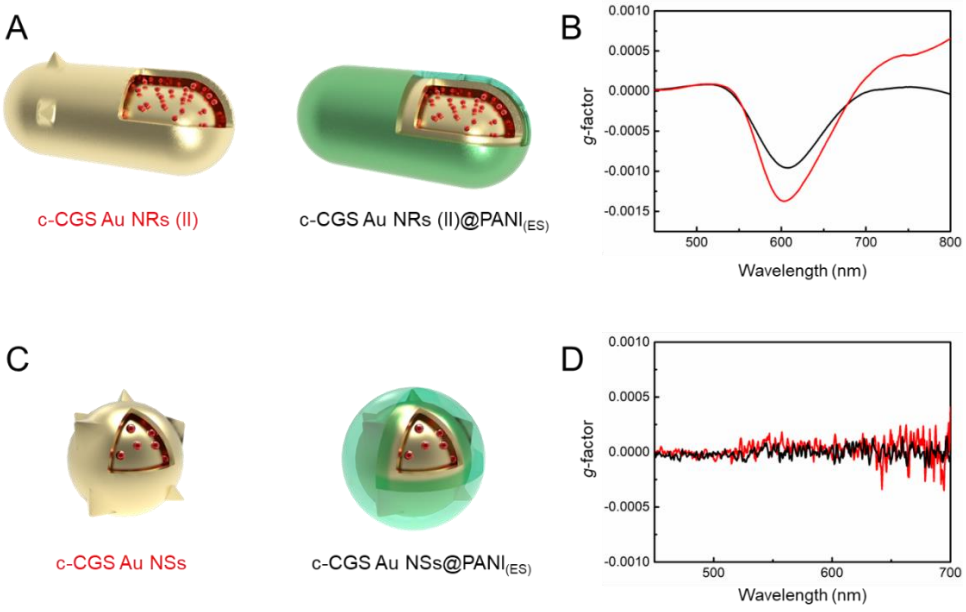


**Figure 3.8** (A) Schematic illustrations and (B) g-factor diagrams of L-c-CGS Au NRs (II) (red curve) and L-c-CGS Au NRs (II)@PANI$_{(ES)}$ (black curve). (C) Schematic illustrations and (D) g-factor diagrams of L-c-CGS Au NSs (red curve) and L-c-CGS Au NSs@PANI$_{(ES)}$ (black curve).

To corroborate that PANI was acting as the cause of the loss of chiral strength within this system, I introduced PANI aqueous solution instead of PANI shell to explain this problem more intuitively (**Figure 3.9A**). As shown in **Figure 3.9B**, both ES and PB states have absorption bands near the T-LSPR region, and the PB state dominates in the absorption intensity, which is obvious for the change in the total absorption (**Figure 3.9C**). However, as an achiral dielectric environment, the PANI solution has little effect on the absorption of circularly polarized light, which may result in a decrease in the apparent g-factor value when the ES was transformed to the PB state (**Figure 3.9D**). Similarly, coating or increasing the thickness of the PANI shell would amplify the total absorption and eventually lead to a decrease in the apparent g-factor. Considering the overall chiral loss due to the PANI layer, c-CGS Au NRs (II) coated with an 11 nm-thick PANI layer was selected for the following studies.

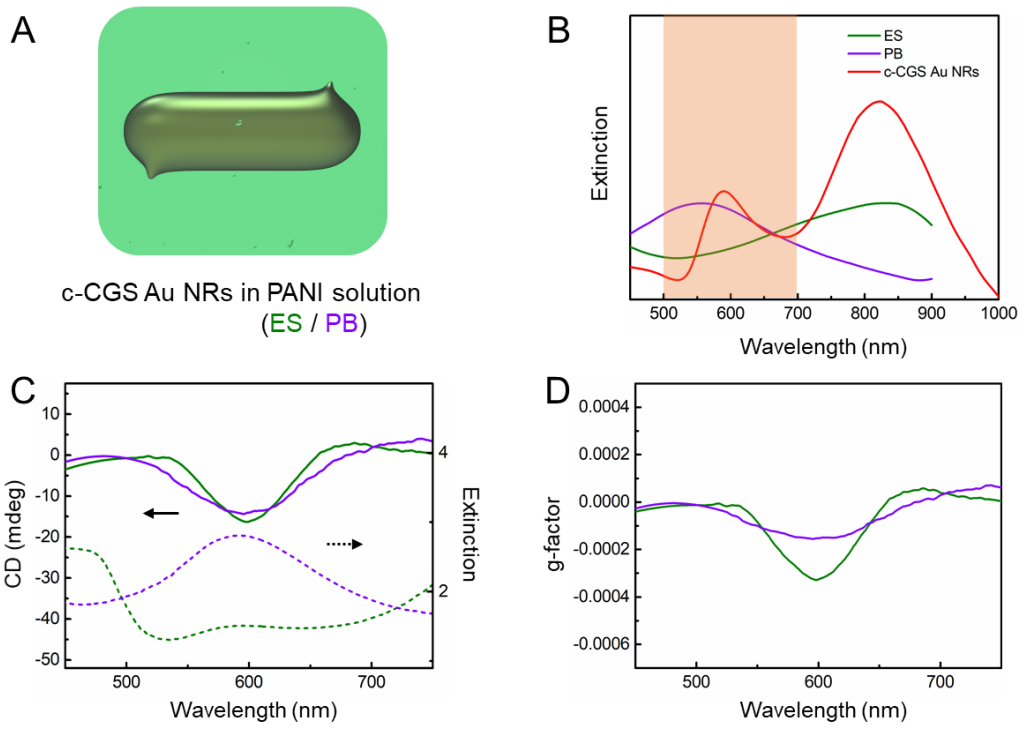


**Figure 3.9** (A) Schematic of c-CGS Au NRs in PANI solution. (B) Extinction spectra of pure PANI solution in the ES (green), PB (purple) states and L-c-CGS Au NRs (red) in water. (C) CD (solid line) and extinction (dashed line) spectra of L-c-CGS Au NRs in solutions with different PANI states (ES: green; PB: purple). (D) g-factor diagrams of L-c-CGS Au NRs in solutions with different PANI states (ES: green; PB: purple).

## pH-Responsive Plasmonic and Plasmon-Induced Chiral Activities

The optimization of the PANI layer encouraged us to explore the pH modulation mechanism in more detail (**Figure 3.10A**). Taking L-c-CGS Au NRs (II)@PANI as an example, its aqueous solution exhibited visual transition from coffee purple to eggplant purple at pH 2 and pH 12, respectively (**Figure 3.10B**), which was attributed to the change in the state of the PANI itself as well as its optical properties.

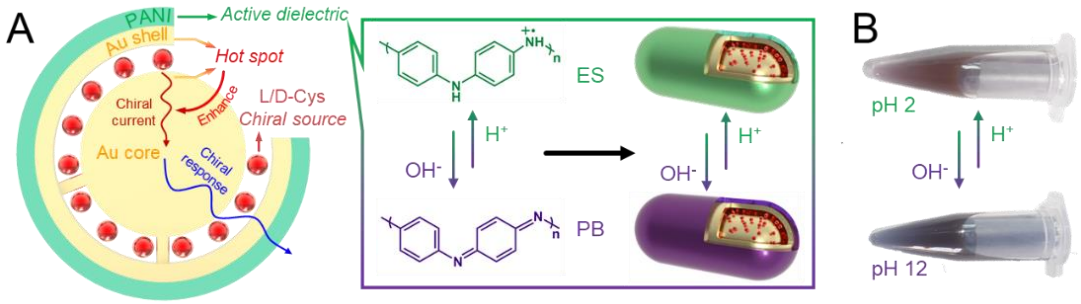


**Figure 3.10** (A) Mechanism of the chiral signal amplification and dielectric environment switching by proton doping and de-doping. (B) Digital image of L-c-CGS Au NRs (II)@PANI solutions at pH 2 and pH 12.

Then, at pH 2, the T-LSPR peak was located at 590 nm, and the corresponding $CD_{T\text{-}LSPR}$ peak was nearby at 601 nm (**Figure 3.11A-D**). Both peaks were narrow, indicating that they were not affected by the ES peak. With the addition of NaOH to the solution, the pH value increased from 2 to 6, indicating that free $H^+$ ions in the solution began to be gradually neutralized (**Figure 3.12**). However, there was no significant shift observed in T-LSPR and its corresponding $CD_{T\text{-}LSPR}$. When the pH value reached 8, both T-LSPR and its corresponding $CD_{T\text{-}LSPR}$ began to shift. This suggests that after all $H^+$ ions in the solution were completely neutralized by $OH^-$, the outermost $H^+$ ions in the PANI "microenvironment" participated in the neutralization, leading to the transition towards the PB state. When the pH value reached 10, both T-LSPR and its corresponding $CD_{T\text{-}LSPR}$ underwent a significant redshift, indicating that the inner $H^+$ ions were gradually involved in neutralization. More and more parts of the PANI layer had started to transition towards the PB state. The change in peak positions was not significant between pH 10 and 12, indicating that the PANI had

completed proton de-doping. Ultimately, the T-LSPR peak red shift was about 57 to 647 nm, while the corresponding $CD_{T\text{-}LSPR}$ peak also completed a similar red shift. Such a significant chiral peak shift cannot be explained solely by the contribution of changes in the dielectric constant and the T-LSPR itself, which suffered from the low sensitivity of T-LSPR, but also by the contribution of the PB state involved in the peak coupling.[27] Similar results were observed in the case of D-c-CGS Au NRs (II)@PANI (**Figure 3.11A, E-G**).

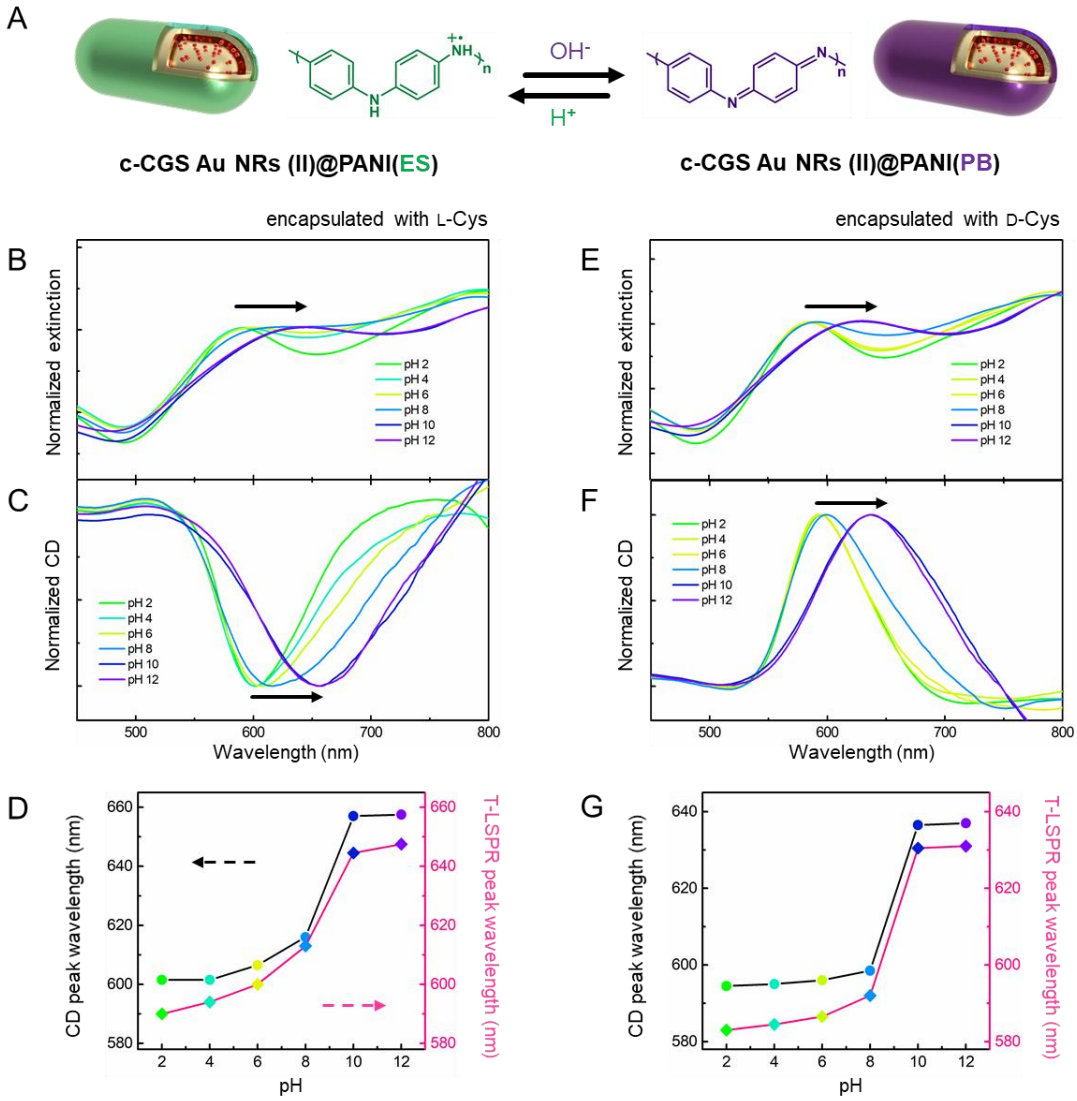


**Figure 3.11** (A) pH-modulated plasmonic and CD switching behavior of c-CGS Au NRs (II)@PANI. (B) Normalized extinction spectra, (C) CD spectra of L-c-CGS Au NRs (II)@PANI and (D) their corresponding peak positions in response to different pH values. (I) Normalized extinction spectra, (J) CD spectra and their corresponding peak positions of D-c-CGS Au NRs (II)@PANI in response to different pH values.

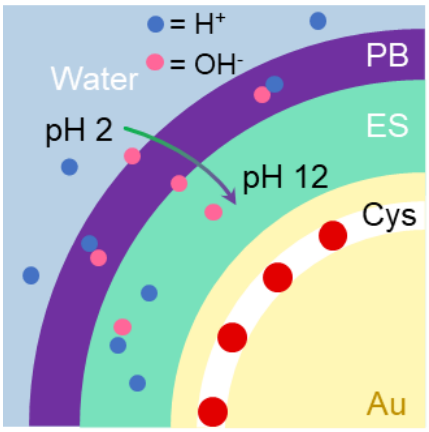


**Figure 3.12** Schematic representation of $OH^-$ entering the PANI microenvironment from solution at different pH values.

## Electrical Potential-Responsive Plasmonic and Plasmon-Induced Chiral Activities

Compared with pH modulation, manipulating the CD peak response with the assistance of electrical potential was definitely a more attractive strategy.[24] To enable voltage manipulation and device fabrication, I employed a Langmuir–Blodgett (LB)-like technique in which a large monolayer film was formed by nanoparticle self-assembly at the water–oil interface. In detail, the hexane was carefully injected onto the surface of the nanorods solution to form an incompatible water–oil interface. Mainly due to the competitive adsorption of newly added ethanol, the surface charge was gradually reduced and the contact angle (less than 90°) of the hydrophilic nanorods tended to be 90°, the nanorods preferentially sank into the interface. After the hexane has evaporated completely, the monolayer film was transferred to the indium tin oxide (ITO) surface (**Figure 3.13A-C**).[28] Subsequently, the functionalized ITO was employed as a working electrode in conjunction with other electrodes to form an electrochemical setup, enabling real-time monitoring of the optical behavior of nanorods during potential switching (**Figure 3.13D**).

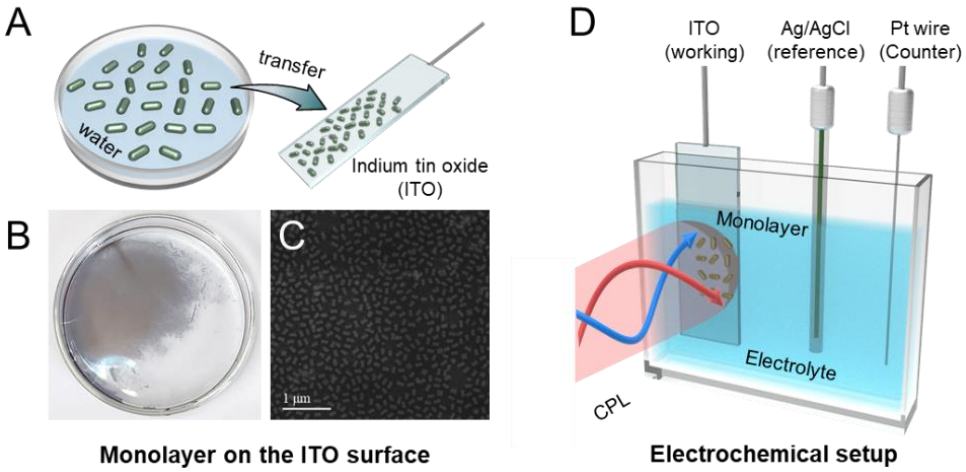


**Figure 3.13** (A) Schematic illustration of the c-CGS Au NRs (II)@PANI monolayer film fabricated and transferred to an ITO surface. (B) Digital photograph of the monolayer film displaced at the water-air interface. (C) SEM image of monolayer film transferred to ITO surface. (D) Schematic illustration of the three-electrode electrochemical cell for the real-time measurement of the extinction and CD spectra of the monolayers on an ITO substrate. The scale bar is 1 μm.

Here, the PANI layer also acted as a physical spacer to avoid strong coupling between particles or between particles and the substrate, allowing the monolayer to display LSPR properties similar to those of discrete nanoparticles. In addition, the LB state exhibited no significant extinction in the visible and near-infrared regions (**Figure 3.14**).


**Figure 3.14** (A) Schematic illustrations and (B) normalized extinction spectra of the conversion between c-CGS Au NSs@PANI$_{(ES)}$ and c-CGS Au NSs@PANI$_{(LB)}$.

Furthermore, taking the L-c-CGS Au NRs (II)@PANI as an example (**Figure 3.15A**), PANI was in the ES state under a higher voltage (0.4 V) and at pH 2. The T-LSPR position of the monolayer was located near 592 nm, while the corresponding CD$_{T\text{-}LSPR}$ peak was located near 602 nm, which were slightly red-shifted compared to the corresponding peak positions of discrete nanoparticles. As the voltage was reduced to −0.3 V, the ES state gradually transitioned to the LB state and the T-LSPR and CD$_{T\text{-}LSPR}$ peaks both underwent the red shifts of 12 and 14 to 604 and 616 nm, respectively (**Figure 3.15B-D**). The peak shapes of the D-c-CGS Au NRs (II)@PANI also showed similar red shift trends (**Figure 3.15E-G**).

It should be noted that for some oriented solid samples, linear dichroism and linear birefringence are the main artifacts that may be observed during CD measurements.[29] To exclude the above effects, I confirmed the consistency of the chiral spectral information from different positions and the *g*-factor values (**Figure 3.16**).

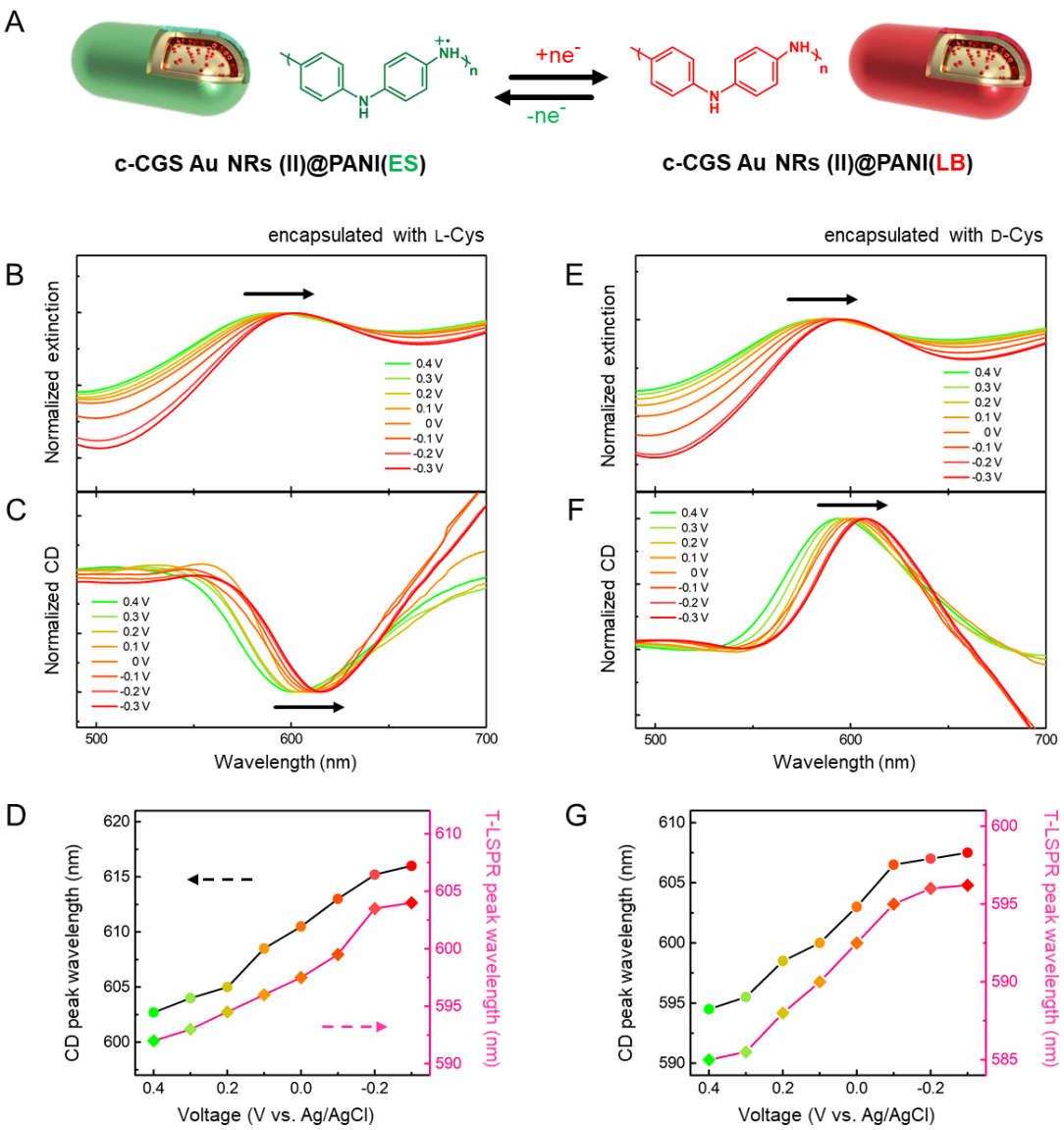


**Figure 3.15** (A) Electrical potential-modulated plasmonic and CD switching behavior of a c-CGS Au NRs (II)@PANI monolayer film. (B) Normalized extinction spectra and (C) CD spectra of L-c-CGS Au NRs (II)@PANI and (D) their corresponding peak positions in response to different voltages. (E) Normalized extinction spectra and (F) CD spectra of D-c-CGS Au NRs (II)@PANI and (G) their corresponding peak positions in response to different environmental pH values.

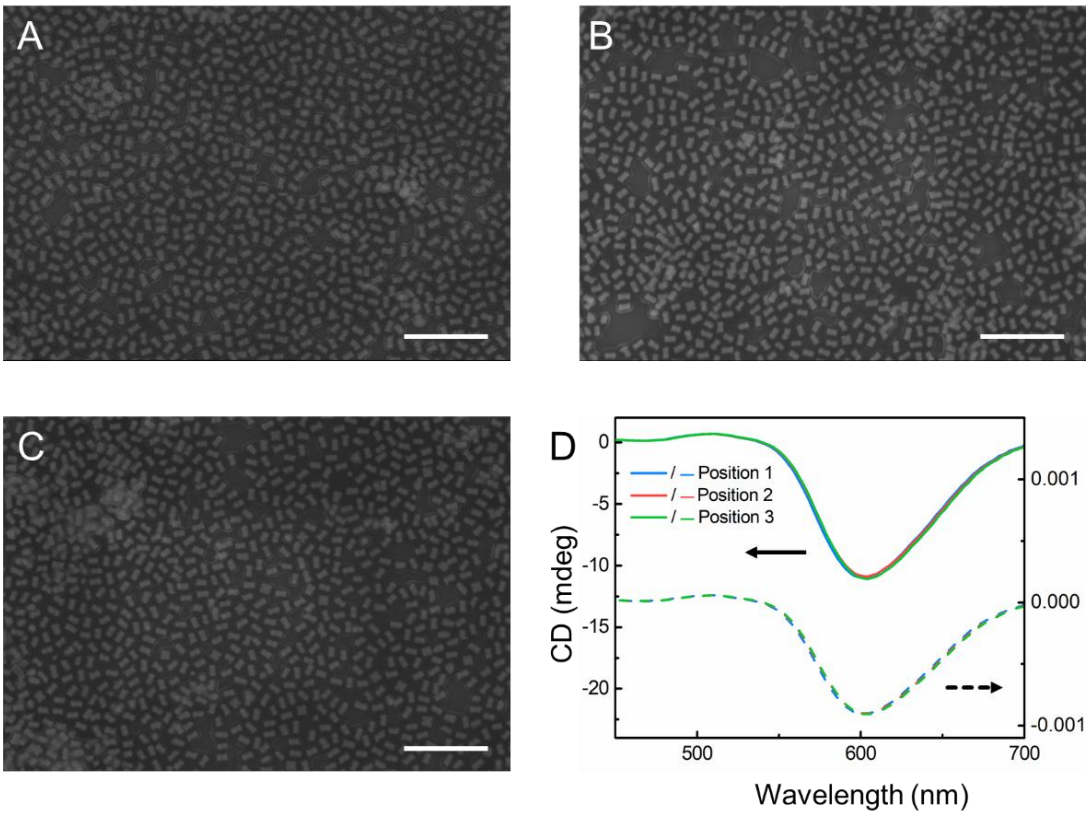


**Figure 3.16** (A-C) SEM images of different probing positions within the L-c-CGS Au NRs (II)@PANI monolayer film. (D) CD spectra of different probe position within the monolayer film. The scale bars are 1 μm.

These results supported our findings regarding the advantages offered by electrical potential as a stimulus source, such as achieving more accurate manipulation while avoiding sudden changes in signal output.

### Stability, Reversibility, and Switching Rates of LSPR and Its Chiroptical Response

To further evaluate the LSPR and $CD_{LSPR}$ dual response, the reversibility and stability of c-CGS Au NRs@PANI were investigated. First, the L-c-CGS Au NRs (II)@PANI solution was switched in turn between pH 2 and pH 12. The shifts in the T-LSPR peak positions and the corresponding $CD_{T\text{-}LSPR}$ peak positions presented good reversibility during the five cycles (**Figure 3.17A**). The electrical potential group also showed stable performance over the same cycles (**Figure 3.17B**). A similar phenomenon also occurred for the prepared D-c-CGS Au NRs(II) PANI (**Figure 3.17C, D**).

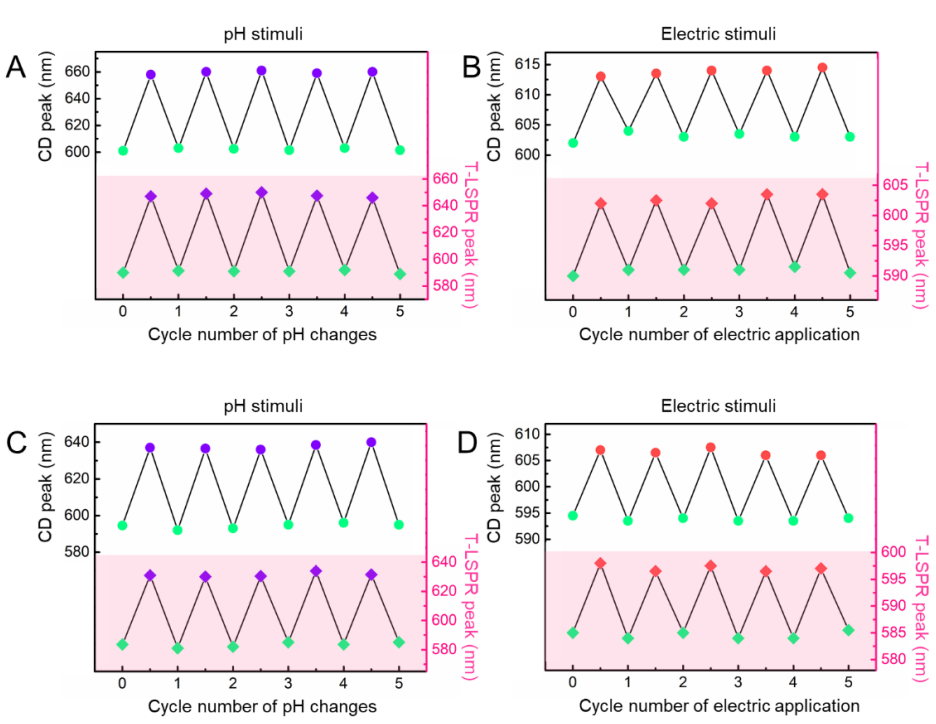


**Figure 3.17** (A) Peak positions corresponding to extinction (squares) and CD (circles) of L-c-CGS Au NRs (II)@PANI at pH 2 (green) or pH 12 (purple) during five cycles. (B) Peak positions corresponding to extinction (squares) and CD (circles) of L-c-CGS Au NRs (II)@PANI monolayers at 0.4 V (green) or −0.3 V (red) during five cycles. (C) Peak positions corresponding to extinction (squares) and CD (circles) of D-c-CGS Au NRs (II)@PANI at pH 2 (green) or pH 12 (purple) during five cycles. (D) Peak positions corresponding to extinction (squares) and CD (circles) of D-c-CGS Au NRs (II)@PANI monolayers at 0.4 V (green) or −0.3 V (red) during five cycles.

The extinction intensity, chiral response, and electrochemical activity curves did not degrade significantly before or after 100 scan cycles, indicating the good reproducibility of the ES and LB states based on electrical potential switching (**Figure 3.18A-C**). Finally, as it was not easy to record instantaneous extinction spectra as in other reports,[25] we measured the falling current stabilization time to reflect the switching rates of the monolayer by using the amperometric *i–t* method at a fixed voltage, which is approximately 500 ms (**Figure 3.18D**).[30] The larger signal shifts from pH modulation and the small range of precise responses from electrical potential modulation reflect the complementary advantages of this material in terms of suitability to different optical scenarios with excellent reversibility and stability.

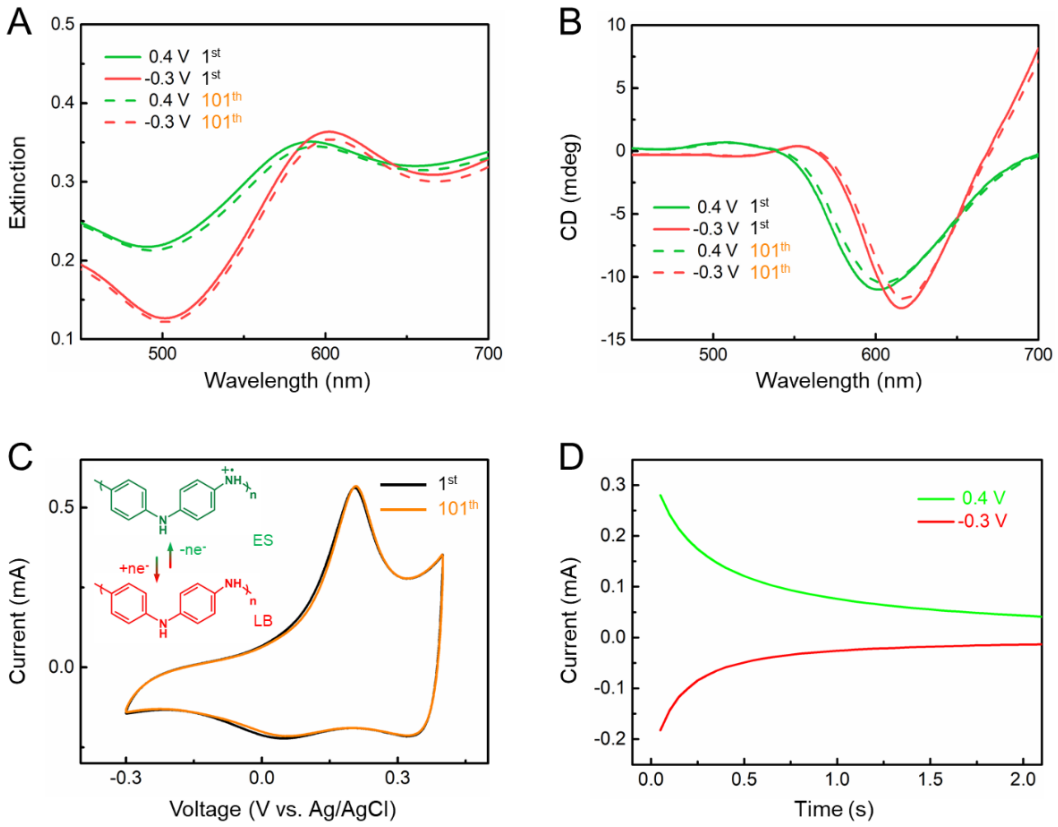


**Figure 3.18** (A) Extinction spectra of L-c-CGS Au NRs (II)@PANI monolayers at 0.4 V (green) and −0.3 V(red) before and after 100 scans. (B) CD spectra of L-c-CGS Au NRs (II)@PANI monolayers at 0.4 V (green) and −0.3 V(red) before and after 100 scans. (C) Cyclic voltammograms of L-c-CGS Au NRs (II)@PANI monolayers before and after 100 scans. (D) Switching time of L-c-CGS Au NRs (II)@PANI monolayers at fixed voltages of 0.4 V (green) and −0.3 V (red).

## 3.4 Conclusion

The c-CGS Au NRs@PANI were successfully prepared using a surfactant-assisted chemical oxidative polymerization method. PANI served as a tunable dielectric layer, imparting active Localized Surface Plasmon Resonance (LSPR) modulation capability to the plasmonic particles. However, it simultaneously reduced asymmetry of the entire system. Therefore, it was crucial to balance these two aspects by adjusting the thickness of PANI. I evaluated the LSPR shift benefits and asymmetry loss associated with three different thicknesses of PANI layers and determined that a PANI layer of 11 nm thickness was most suitable for active chiral plasmon studies. Subsequently, in the case of pH modulation, as the solution environment transitioned from pH 2 to pH 12, $CD_{T\text{-}LSPR}$ underwent a significant shift of 60 nm following T-LSPR. The corresponding solution color changed from brown to eggplant purple. Before initiating the potential modulation, I self-assembled the plasmonic particles at the oil-water interface to obtain a large-area monolayer film, which was then transferred onto the ITO surface as the working electrode. By gradually decreasing the potential from 0.4 V with a step size of 0.1 V to -0.3 V, $CD_{T\text{-}LSPR}$ experienced a slight shift of 12 nm following T-LSPR. Meanwhile, the c-CGS Au NRs (II)@PANI showed excellent stability and reversibility, the ability to switch optical features in real time, and flexible designability and processability. The above properties indicate that a similarly well-defined discrete active plasmonic structure could be a strong candidate for the fabrication of novel optical devices, such as optical switches, transducers, and filters.

## 3.5 References


[1] Im, S. W.; Ahn, H. Y.; Kim, R. M.; Cho, N. H.; Kim, H.; Lim, Y. C.; Lee, H. E.; Nam, K. T. Chiral Surface and Geometry of Metal Nanocrystals. *Adv. Mater.* **2019**, *32*, 1905758.

[2] Ben-Moshe, A.; Maoz, B. M.; Govorov, A. O.; Markovich, G. Chirality and Chiroptical Effects in Inorganic Nanocrystal Systems with Plasmon and Exciton Resonances. *Chem. Soc. Rev.* **2013**, *42*, 7028-7041.

[3] Severoni, E.; Maniappan, S.; Liz-Marzán, L. M.; Kumar, J.; García de Abajo, F. J.; Galantini, L. Plasmon-Enhanced Optical Chirality through Hotspot Formation in Surfactant-Directed Self-Assembly of Gold Nanorods. *ACS Nano* **2020**, *14*, 16712-16722.

[4] Nguyen, L.; Dass, M.; Ober, M. F.; Besteiro, L. V.; Wang, Z. M.; Nickel, B.; Govorov, A. O.; Liedl, T.; Heuer-Jungemann, A. Chiral Assembly of Gold-Silver Core-Shell Plasmonic Nanorods on DNA Origami with Strong Optical Activity. *ACS Nano* **2020**, *14*, 7454-7461.

[5] Wu, Z.; Zheng, Y. Moiré Chiral Metamaterials. *Adv. Opt. Mater.* **2017,** *5*, 1700034.

[6] Wang, X.; Tang, Z. Circular Dichroism Studies on Plasmonic Nanostructures. *Small* **2017**, *13*, 1601115.

[7] Wu, Z.; Chen, X.; Wang, M.; Dong, J.; Zheng, Y. High-Performance Ultrathin Active Chiral Metamaterials. *ACS Nano* **2018**, *12*, 5030-5041.

[8] Zhou, C.; Duan, X.; Liu, N. DNA-Nanotechnology-Enabled Chiral Plasmonics: From Static to Dynamic. *Acc. Chem. Res.* **2017**, *50*, 2906-2914.

[9] Man, T.; Ji, W.; Liu, X.; Zhang, C.; Li, L.; Pei, H.; Fan, C. Chiral Metamolecules with Active Plasmonic Transition. *ACS Nano* **2019**, *13*, 4826-4833.

[10] Lan, X.; Liu, T.; Wang, Z.; Govorov, A. O.; Yan, H.; Liu, Y. DNA-Guided Plasmonic Helix with Switchable Chirality. *J. Am. Chem. Soc.* **2018**, *140*, 11763-11770.

[11] Nguyen, M.-K.; Kuzyk, A. Reconfigurable Chiral Plasmonics beyond Single Chiral Centers. *ACS Nano* **2019**, *13*, 13615-13619.

[12] Querejeta-Fernández, A.; Chauve, G.; Methot, M.; Bouchard, J.; Kumacheva, E. Chiral Plasmonic Films Formed by Gold Nanorods and Cellulose Nanocrystals. *J. Am. Chem. Soc.* **2014**, *136*, 4788-4793.

[13] Querejeta-Fernández, A.; Kopera, B.; Prado, K. S.; Klinkova, A.; Methot, M.; Chauve, G.; Bouchard, J.; Helmy, A. S.; Kumacheva, E. Circular Dichroism of Chiral Nematic Films of Cellulose Nanocrystals Loaded with Plasmonic Nanoparticles. *ACS Nano* **2015**, *9*, 10377-10385.

[14] Schreiber, R.; Luong, N.; Fan, Z.; Kuzyk, A.; Nickels, P. C.; Zhang, T.; Smith, D. M.; Yurke, B.; Kuang, W.; Govorov, A. O.; Liedl, T. Chiral Plasmonic DNA Nanostructures with Switchable Circular Dichroism. *Nat. Commun.* **2013**, *4*, 2948.

[15] Probst, P. T.; Mayer, M.; Gupta, V.; Steiner, A. M.; Zhou, Z.; Auernhammer, G. K.; König, T. A. F.; Fery, A. Mechano-Tunable Chiral Metasurfaces via Colloidal Assembly. *Nat. Mater.* **2021**, *20*, 1024-1028.

[16] Nakamura, S.; Mitomo, H.; Yonamine, Y.; Ijiro, K. Salt-Triggered Active Plasmonic Systems Based on the Assembly/Disassembly of Gold Nanorods in a DNA Brush Layer on a Solid Substrate. *Chem. Lett.* **2020**, *49*, 749-752.

[17] Jiang, N.; Zhuo, X.; Wang, J. Active Plasmonics: Principles, Structures, and Applications. *Chem. Rev.* **2017**, *118*, 3054-3099.

[18] Liu, B.; Lu, X.; Qiao, Z.; Song, L.; Cheng, Q.; Zhang, J.; Zhang, A.; Huang, Y.; Chen, T. pH and Temperature Dual-Responsive Plasmonic Switches of Gold Nanoparticle Monolayer Film for Multiple Anticounterfeiting. *Langmuir* **2018**, *34*, 13047-13056.

[19] Iida, R.; Mitomo, H.; Niikura, K.; Matsuo, Y.; Ijiro, K. Two-Step Assembly of Thermoresponsive Gold Nanorods Coated with a Single Kind of Ligand. *Small* **2018**, *14*, 1704230.

[20] Baker, C. O.; Huang, X.; Nelson, W.; Kaner, R. B. Polyaniline Nanofibers: Broadening Applications for Conducting Polymers. *Chem. Soc. Rev.* **2017**, *46*, 1510-1525.

[21] Jiang, N.; Shao, L.; Wang, J. (Gold Nanorod Core)/(Polyaniline Shell) Plasmonic Switches with Large Plasmon Shifts and Modulation Depths. *Adv. Mater.* **2014**, *26*, 3282-3289.

[22] Lin, H.; Song, L.; Huang, Y.; Cheng, Q.; Yang, Y.; Guo, Z.; Su, F.; Chen, T. Macroscopic Au@PANI Core/Shell Nanoparticle Superlattice Monolayer Film with Dual-Responsive Plasmonic Switches. *ACS Appl. Mater. Interfaces* **2020**, *12*, 11296-11304.

[23] Jeon, J.-W.; Zhou, J.; Geldmeier, J. A.; Ponder, J. F.; Mahmoud, M. A.; El-Sayed, M.; Reynolds, J. R.; Tsukruk, V. V. Dual-Responsive Reversible Plasmonic Behavior of Core–Shell Nanostructures with pH-Sensitive and Electroactive Polymer Shells. *Chem. Mater.* **2016**, *28*, 7551-7563.

[24] Jeon, J.-W.; Ledin, P. A.; Geldmeier, J. A.; Ponder, J. F.; Mahmoud, M. A.; El-Sayed, M.; Reynolds, J. R.; Tsukruk, V. V. Electrically Controlled Plasmonic Behavior of Gold Nanocube@Polyaniline Nanostructures: Transparent Plasmonic Aggregates. *Chem. Mater.* **2016**, *28*, 2868-2881.

[25] Lu, W.; Jiang, N.; Wang, J. Active Electrochemical Plasmonic Switching on Polyaniline-Coated Gold Nanocrystals. *Adv. Mater.* **2017**, *29*, 1604862.

[26] Lu, Y.; Lam, S. H.; Lu, W.; Shao. L.; Chow, T. H.; Wang, J. All-State Switching of the Mie Resonance of Conductive Polyaniline Nanospheres. *Nano Lett.* **2022**, *22*, 1406-1414.

[27] Chen, H.; Shao, L.; Li, Q.; Wang, J. Gold Nanorods and Their Plasmonic Properties. *Chem. Soc. Rev.* **2013**, *42*, 2679-2724.

[28] Lu, X.; Huang, Y.; Liu, B.; Zhang, L.; Song, L.; Zhang, J.; Zhang, A.; Chen, T. Light-Controlled Shrinkage of Large-Area Gold Nanoparticle Monolayer Film for Tunable SERS Activity. *Chem. Mater.* **2018**, *30,* 1989-1997.

[29] Merten, C.; Kowalik, T.; Hartwig, A. Vibrational Circular Dichroism Spectroscopy of Solid Polymer Films: Effects of Sample Orientation. *Appl. Spectrosc*. **2008**, *62*, 901-905.

[30] Kaissner, R.; Li, J.; Lu, W.; Li, X.; Neubrech, F.; Wang, J.; Liu, N. Electrochemically Controlled Metasurfaces with High-contrast Switching at Visible Frequencies. *Sci. Adv.* **2021**, *7*, eabd9450.

# *Chapter 4*

## *Preparation of Intrinsic Chiral Nanostructures by Gold Octahedral Nanoframes as Seeds*

## 4.1 Introduction

Metal NPs exhibiting inherent 3D chiral morphologies often display enhanced chiroptical activity.[1] However, this introduces a conceptually significant challenge in wet chemical synthesis methods, namely, inducing chiral distortions when metal atoms deposit on the surface of achiral seed.[2] The current consensus strategy is to introduce chiral molecules (such as amino acids or peptides) during the regrowth process, serving as triggers for atomically asymmetric deposition. Nam et al. were the first to provide a detailed description of the two main steps in this chiral growth process: 1) formation of high-Miller-index surfaces during excessive growth of seed; 2) enantioselective interactions between chiral molecules and these surfaces, thereby altering the deposition orientation of subsequent atoms.[3] Hammer et al. employed density-functional theory (DFT) to elucidate the role of the chiral molecule (Cys) in the process of chiral growth of Au NPs.[4] They theoretically demonstrated that the adsorption orientation of L-Cys and D-Cys on the same high-Miller-index Au surface (321) differs, thereby driving the asymmetric growth. Based on these principles, an increasing number of achiral Au NPs have been introduced as seeds, including Au NRs,[5-7] gold nanoplates,[8, 9] gold nanotriangles,[10, 11] and gold nanodisks.[12] Liz-Marzán et al. recently reported another instance of inducing ordered chiral growth of particles using chiral micelles.[13] By adsorbing chiral micelles on the surface of achiral Au NRs, they guided the seed growth, resulting in chiral Au NRs with a helical texture on the surface. These structures exhibited pronounced chirality, dependent on the dimensions of the Au NRs. Additionally, there are reports suggesting that CPL can participate in the regulation of chiral growth. Kotov et al. successfully obtained chiral gold nanostructures by simply irradiating a mixture of chloroauric acid and sodium citrate with CPL.[14]

However, despite substantial efforts dedicated to synthesizing inherently chiral nanostructures, progress in this field has been relatively slow. Numerous questions remain unanswered, such as the factors influencing the high chiroptical properties (*g*-factor) of chiral plasmonic nanostructures.[15] Is it primarily dictated by the size

and shape of the seed particles, or is it associated with the quantity, length, or depth of the helix formed after growth? Addressing these inquiries may necessitate the introduction of more complex, multi-level particles as seeds for chiral growth, allowing for comprehensive and integrated considerations.

In this chapter, I introduced a 3D gold octahedral nanoframe (Au ONF) serving as colloidal seeds for chiral growth. The frame possesses 12 arms of equal length, akin to integrating 12 Au NRs within a single frame. Each arm is available for chiral growth, theoretically endowing the resulting particles with significant chiral activity. The construction of such intricate chiral structures may contribute to understanding the origin of plasmonic chiral activity.

## 4.2 Experimental Section

### Materials

$HAuCl_4 \cdot 3H_2O$ (99.9%), $NaBH_4$ (99.0%), AA (99.0%), L-Glutathione reduced (L-Gsh, ≥98.0%) and sodium iodide (NaI, ≥99.5%) were bought from Sigma-Aldrich. CTAB (>98.0%), CTAC (>95.0%), $AgNO_3$ (99.8%), hydrogen hexachloroplatinate(IV) hexahydrate ($H_2Cl_6Pt \cdot 6H_2O$, 99.9%) and HCl (35~37 wt % in water) were purchased from FUJIFILM Wako Pure Chemical Corp. (Osaka, Japan). Ultrapure water was used to prepare all solutions for the experiments (Milli-Q reference system).

### Characterization

UV−vis spectra were recorded using a Jasco V-730 spectropolarimeter. Field-emission scanning electron microscopy (SEM) measurements were carried out using an ultimate field emission scanning electron SU-8230 (Hitachi High-Tech, Tokyo, Japan) at an acceleration voltage of 8 kV. Scanning transmission electron microscope (STEM) observations were carried out using a HD-2000 (Hitachi High-Tech, Tokyo, Japan) with a 200 kV accelerating voltage.

### Preparation of Gold octahedral nanoparticle (Au ONP)

CTAC-coated Au ONP were prepared according to the seed-mediated growth method.[16] First, Au seeds were prepared by injecting fresh ice-cold $NaBH_4$ aqueous solution (225 μL, 20 mM) into a mixture of $HAuCl_4$ (125 μL, 10 mM) and CTAC (2.5 mL, 0.2 M) solution with vigorous stirring for 2 min, and the mixture was let stand undisturbed (30 °C, 1 h) to allow the excess $NaBH_4$ to age out.

CTAC (5 mL, 0.2 M), water (4.5 mL), HAuCl4 (250 μL, 10 mM) solution, KI (5 μL, 1 mM), and AA (220 μL, 40 mM) were mixed in a vial noted as A growth solution. CTAC (40 mL, 0.2 M), water (36 mL), $HAuCl_4$ (2 mL, 10 mM) solution, KI (40 μL, 1 mM), and AA (1.76 mL, 40 mM) were mixed in a vial noted as B growth solution. Next, Au seeds (25 μL) were added to the solution in vial A with shaking until the solution color turned light pink. Then the solution in vial A (200 μL) was transferred to vial B with thorough mixing for 10 s. The solution in vial B was left undisturbed

for 15 min for particle growth. Finally, homogeneous CTAC-coated Au ONP were redispersed in CTAB solution (20 mL, 50 mM) after centrifugation twice (3405*g,* 10 min).

### Preparation of Au ONP@Platinum (Au ONP@Pt)

The CTAB (8 mL, 50 mM), Au ONP (2 mL), NaI (115 μL, 5 mM), $AgNO_3$ (50 μL, 1 mM), AA (480 μL, 0.1 M) were added sequentially into a vial and then incubated (70 °C, 1 h). Subsequently, HCl (480 μL, 0.1 M) and $H_2PtCl_6$ (400 μL, 2 mM) were injected into the vial with gentle shaking. The solution was incubated again (70 °C, 3 h) to obtain Au ONP@Pt. The solution was then centrifuged twice (6540*g*, 10 min) and finally dispersed into CTAB solution (10 mL, 50 mM).

### Preparation of PtAu octahedral nanoframe (PtAu ONF)

Pt ONF were obtained by selective etching of Au ONP@Pt. Specifically, Au ONP@Pt (8 mL), NaI (88 μL, 5 mM), and $HAuCl_4$ (500 μL, 2 mM) were mixed and incubated (50 °C, 2 h). Subsequently, the above solution was cooled to 30 °C. Then above Pt ONF solution was centrifuged twice (6540*g*, 10 min) and finally dispersed into CTAB solution (8 mL, 1 mM).

### Preparation of Au ONF and Chiral Au ONF (c-Au ONF)

Au ONF was obtained by one-step growth of PtAu ONF. Specifically, $H_2O$ (680 μL), CTAB (120 μL, 50 mM), $HAuCl_4$ (30 μL, 2 mM), AA (20 μL, 0.1 M), L-Gsh (20 μL) and Pt NORF (200 μL) were added to the vial. Then leave the solution to incubate (30 °C, 1 h). c-Au ONF was obtained by multi-step growth of Au ONF. Specifically, after Au ONF growth was completed, $HAuCl_4$ (6 μL, 2 mM) was added to the above solution every 30 min. The reaction was completed by waiting 30 min after the 5th addition. Maintain the concentration of L-Gsh in the final solution at 32 μM. Then above Au ONF and c-Au ONF solution were centrifuged twice (6540*g*, 10 min) and finally dispersed into CTAB solution (1 mL, 50 mM).

## 4.3 Results and Discussion

### Design of Synthetic Pathways for Chiral Gold Octahedral Nanoframe

I devised a wet chemical approach for the stepwise construction for c-Au ONF (**Figure 4.1**). This approach commences with uniformly shaped and sized Au ONP as initial seeds, involving five distinct chemical reaction steps: (1) Coating with a thin Ag layer; (2) Edge-selective deposition of Pt; (3) Selective etching of internal Au; (4) Concentric growth of Au; and (5) Chiral growth of Au. In the first step, a thin Ag layer was initially coated on the surface of the Au ONP (Au ONP@Ag). This Ag layer served as an electron transport channel, inducing the reduction of Pt through electron exchange between Ag and subsequent $Pt^{4+}$ ions.[17] In the second step, assisted by $Ag^{+}$ ions, Pt underwent selective deposition along the 12 edges and 6 vertices of the Au ONP (surfaces with energy higher than the surfaces of the remaining 8 facets). Due to a substantial lattice constant mismatch between Pt and Au (approximately 4.8%),[18] this exhibited a Volmer-Weber growth mode, where Pt atoms formed numerous islands at deposition sites.[19] With the continuous progression of the deposition reaction, these numerous islands gradually grew into columnar islands and converged over time, ultimately forming a rough surface (Au ONP@Pt). In the third step, the etching conditions were induced by using $Au^{3+}$ ions and CTAB, resulting in the slow and selective etching of the internal Au ONP. This process led to the formation of a PtAu frame with an octahedral configuration (PtAu ONF). Traces of Au atoms near the Pt frame remained intact, possibly due to the protection provided by Pt in that region.[20] In the fourth step, a growth solution was introduced with ascorbic acid, L-Gsh, and $Au^{3+}$ ions, forming an $Au^{+}$-S complex. Compared to $Au^{+}$, this complex exhibited a lower reduction potential, leading to a deceleration in the reduction rate.[21] Following the introduction of PtAu ONF, Au atoms deposited slowly and concentrically on the frame, resulting in the formation of Au ONF. As for the fifth step, a low dose of $Au^{3+}$ was gradually added to the solution. Upon reduction to Au atoms, it competed with L-Gsh for fresh binding sites. This growth trend holds the potential to induce the formation of chiral morphology (c-Au ONF).

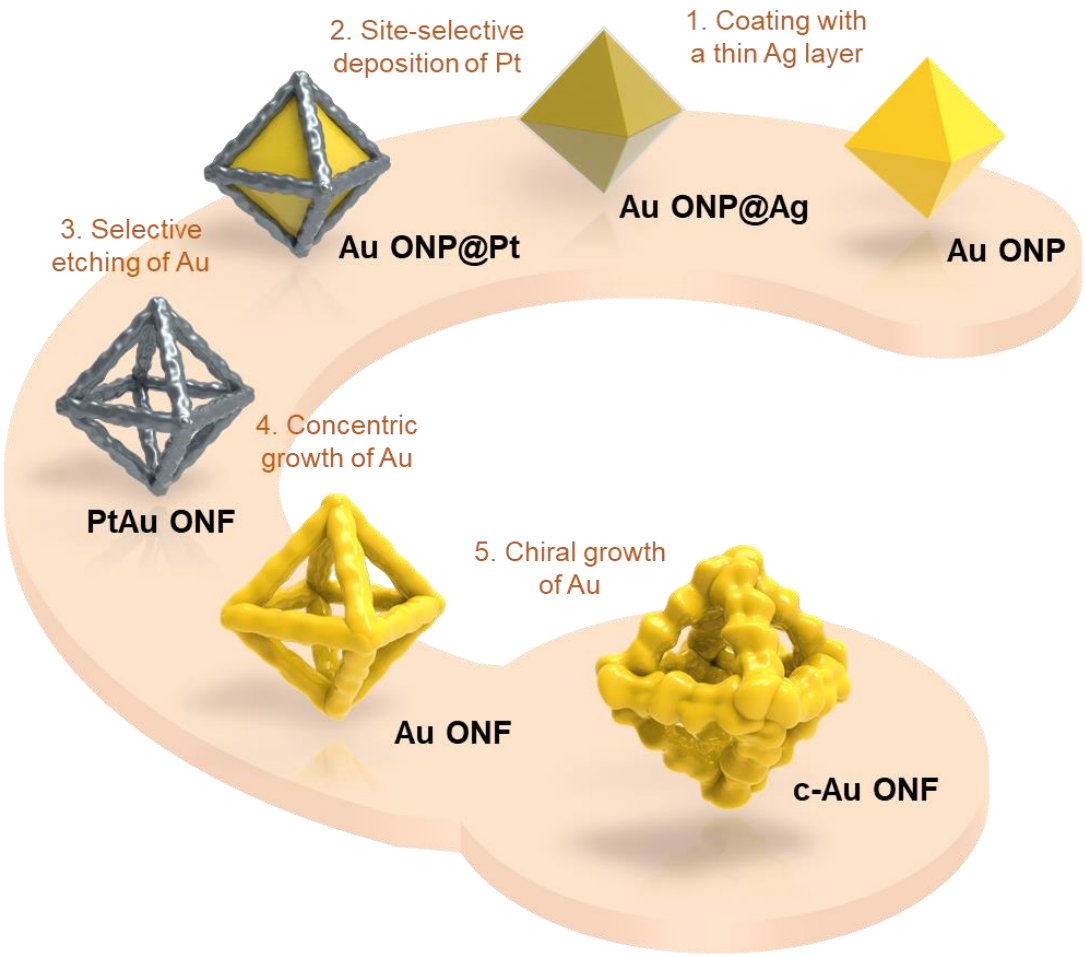


**Figure 4.1** Multiple synthetic pathways for c-Au ONF.

## Synthesis Mechanism and Characterization of Particles at Each Step

SEM images (**Figure 4.2A-F**) and extinction spectra (**Figure 4.2G**) provided essential features of the corresponding structures. The seed Au ONP exhibited high uniformity, with a measured edge length of 90 nm, displaying a pronounced LSPR peak at 610 nm. Upon the deposition of a thin Ag layer, although there was a slight increase in the overall structural dimensions, the smaller dielectric constant of silver leads to a 5 nm blue shift in the corresponding LSPR peak.[22] Subsequent selective deposition of Pt caused the LSPR peak to red-shift from 605 nm to 695 nm, primarily attributed to the effective plasmonic coupling between Pt frame and Au ONP inside.[23] After the selective etching of the internal gold region in the Au ONP@Pt, no distinct LSPR bands were observed, as Pt exhibits minimal optical activity in the visible and near-infrared spectral windows.[24] Moreover, the residual Au free electron population on the Pt framework was insufficient to induce their collective oscillations. With the uniform deposition of Au atoms on the PtAu framework, a near-infrared region LSPR peak (L-LSPR) emerged, attributed to the long-range oscillations of free electrons on the entire Au NOF surface, while T-LSPR around 500 nm was ascribed to short-range dipole oscillations. With the continued deposition of gold atoms, leading to an overall increase in the frame thickness, the T-LSPR peak of c-Au NOF red-shifted to 540 nm, displaying a pronounced peak shape, while the L-LSPR peak blue-shifted to 864 nm. The surface of the structure (s-c-Au ONF, "s" means suspected) after L-Gsh-mediated growth of Au ONF exhibited a distinctive sawtooth morphology, which could be considered as an initial sign of preliminary chiral twisting. Achieving optimal twisting may have required precise control over the amounts of $Au^{3+}$ ions and L-Gsh utilized during the growth process.

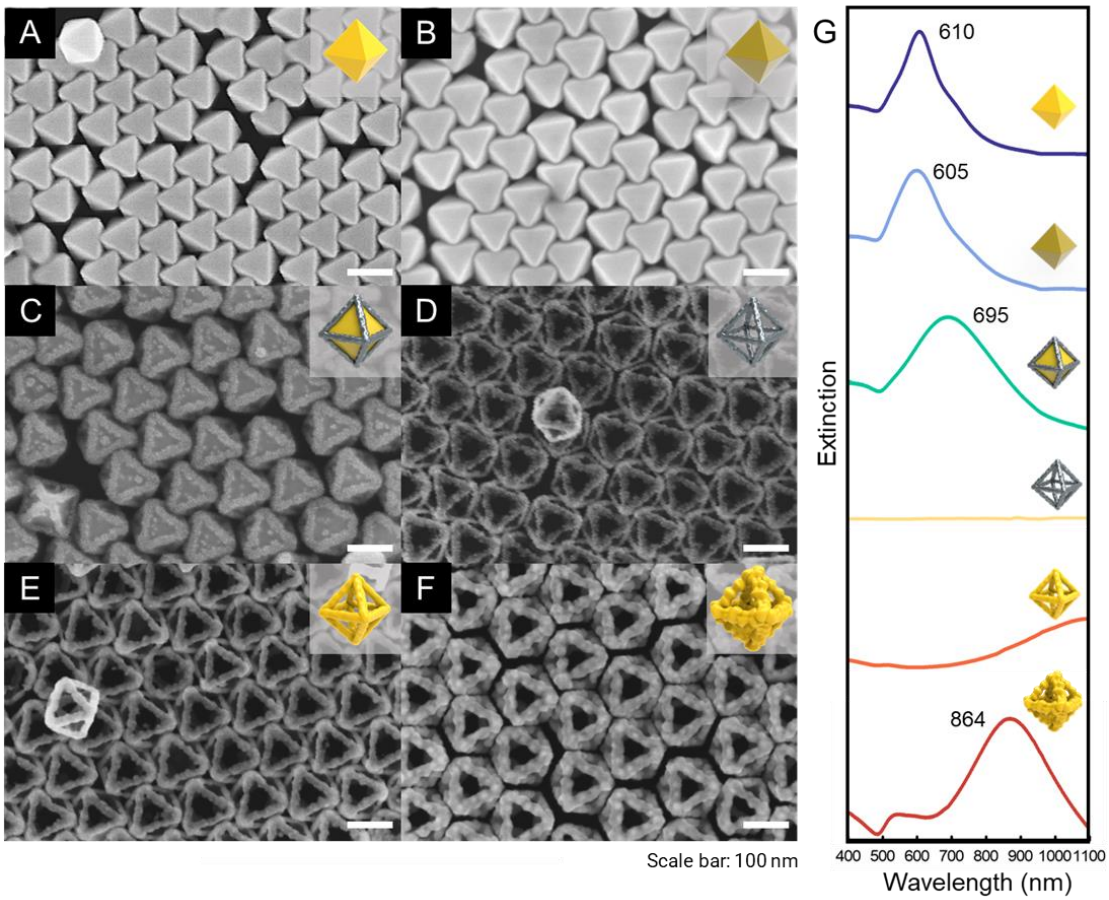


**Figure 4.2** SEM images of (A) Au ONP, (B) Au ONP@Ag, (C) Au ONP@Pt, (D) PtAu ONF, (E) Au ONF and (F) c-Au ONF. (G) Extinction spectra of Au ONP, Au ONP@Ag, Au ONP@Pt, PtAu ONF, Au ONF and s-c-Au ONF, from top to bottom. The illustration shows the corresponding structure. The scale bars are 100 nm.

## Optimizing Chiral Growth of the Gold Octahedral Nanoframe

In the preparation of chiral structures, the use of stepwise addition of low concentrations of $Au^{3+}$ ions for multi-step growth was considered a safe and effective approach.[25] The chiral morphology and chiroptical activity of particles could be gradually optimized in a relatively mild growth environment. In contrast, in a single-step growth strategy, the transient high concentration of $Au^{3+}$ ions in the solution may induce side reactions, such as L-Gsh potentially inducing self-assembly of Au atoms into wire-like structures.[9] In this research project, due to the significant difference in lattice constants between Au and Pt, Au atoms struggled to rapidly deposit on the Pt framework surface, making them more prone to self-assemble into Au wires (**Figure 4.3**). In the multi-step growth strategy, the concentration of $Au^{3+}$ in the solution remained consistently low, effectively inhibiting the formation of gold nanowires. Meanwhile, noticeable changes in the frame morphology were observed (**Figure 4.4**).

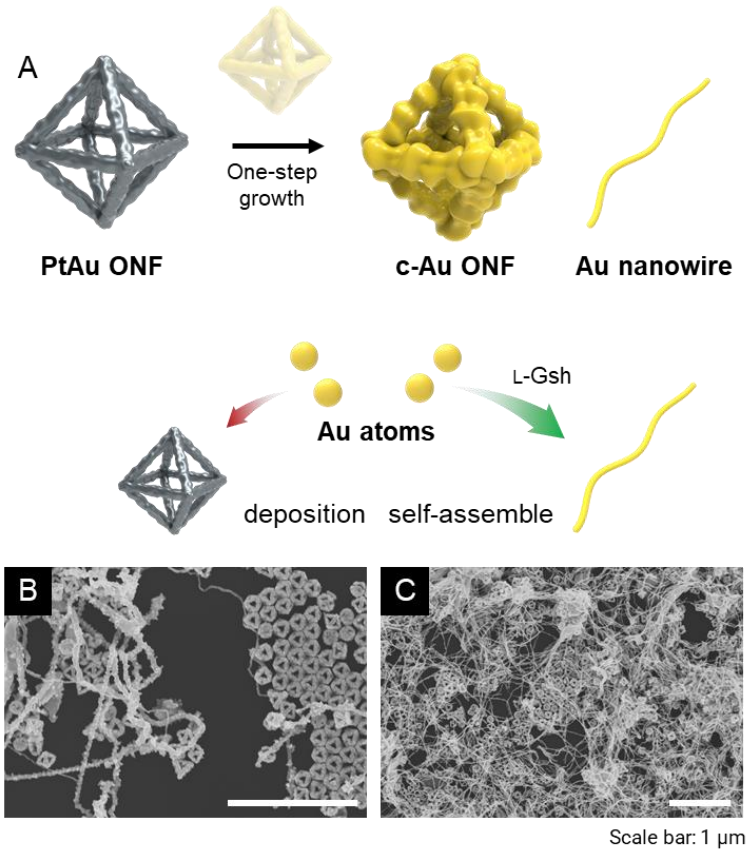


**Figure 4.3** Schematic illustration (A) and SEM images (B, C) of single-step growth with possible byproducts (gold nanowire). The scale bars are 1 μm.

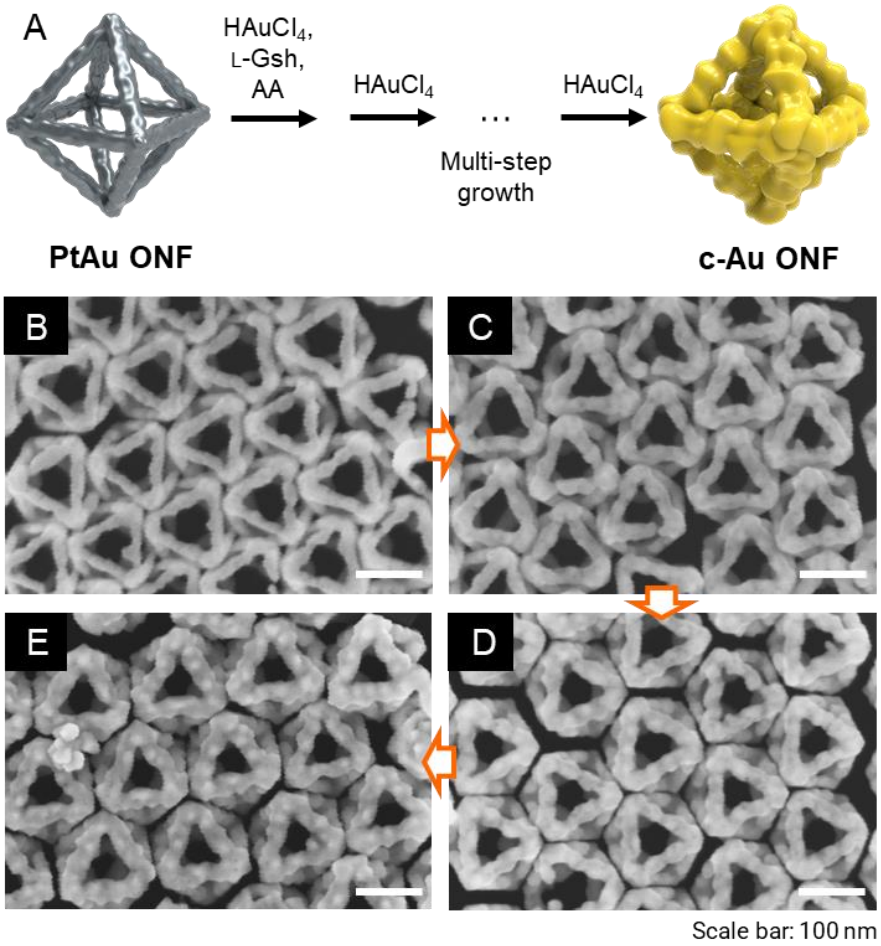


**Figure 4.4** Schematic illustration (A) of multi-step growth. SEM images of first growth (B), second growth (C), third growth (D) and fifth growth (E). The scale bars are 100 nm.

The impact of L-Gsh concentration on the final morphology of the particles was also significant (**Figure 4.5**). When L-Gsh was not used, gold atoms predominantly selectively deposited at the vertices of the frame, ultimately forming a 3D Au NS hexamer. This was attributed to the gold residues at the vertices after etching, serving as active sites for gold deposition during the growth period.[20] When adding L-Gsh (1 μM), the growth mode of the particles exhibited a tendency towards isotropic growth. This phenomenon may be attributed to the formation of $Au^{+}$-S complexes between $Au^{+}$ and L-Gsh, resulting in a decrease in reduction potential and a slowdown in the reduction rate.[21] Additionally, the residual gold, previously serving as an active site, might have been silenced by the free L-Gsh in the solution.

By further increasing the L-Gsh concentration, the particle morphology gradually exhibited a sawtooth pattern. However, when the concentration reached its maximum value (64 μM), this phenomenon disappeared, and gold atoms could not deposit on the particle surface. This was attributed to the competition between gold atoms and L-Gsh for the fresh surface sites on the particles.[26] Specifically, the flat surface of the particles could be regarded as a static valley, while the ridges, due to their larger curvature and lower ligand packing density, became favorable sites for the easy deposition of gold atoms. Subsequently, the exposed surface after growth could once again serve as new sites occupied by ligands and gold atoms. It was worth noting that the formation of ridges consumed the surrounding gold precursors, leading to the sequential appearance of ridges and valleys, resulting in a sawtooth-shaped edge.[27] This morphological distortion could be considered a precursor to chiral twists, and the further optimization of experimental parameters required consideration of the chiral optical activity.

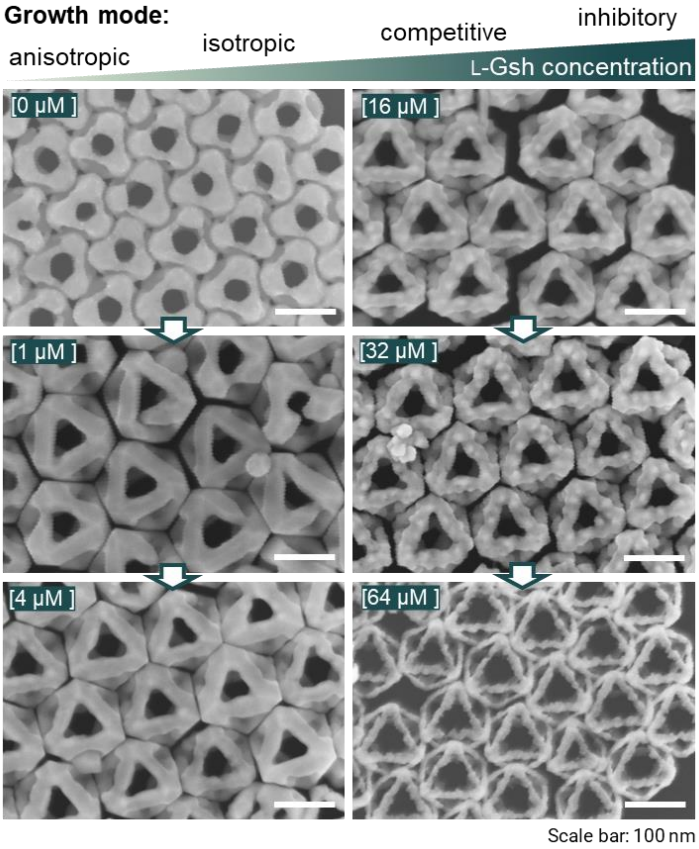


**Figure 4.5** SEM images of the final particle morphology resulting from different L-Gsh concentrations. The scale bars are 100 nm.

The s-c-Au ONF, suspected of having a twisted morphology (synthesized under 32 μM L-Gsh, **Figure 4.6A**), underwent CD testing. However, the excessively noisy chiral signals indicated that the frame's morphology lacked distinct chiral features, or its twisted structure was not continuous (**Figure 4.6B**). Possible reasons for this include the following: 1) The rough surface of the Au ONF or PtAu ONF used as seeds resulted in the discontinuity of chiral morphology during subsequent growth. Previous studies have indicated that chiral growth typically occurs on crystal faces with well-defined high-Miller-indices.[3] The formation of the Pt framework, originating from island-like growth of Pt on the Au octahedral surface, likely posed challenges for the directed deposition of subsequent Au atoms.; 2) Further optimization of chiral conditions is required. It is well-known that the growth environment for chiral morphology imposes strict requirements. Under the current conditions, a more refined control, considering the results from circular dichroism spectroscopy, should be applied to L-Gsh, CTAB, ascorbic acid, and even the growth temperature.

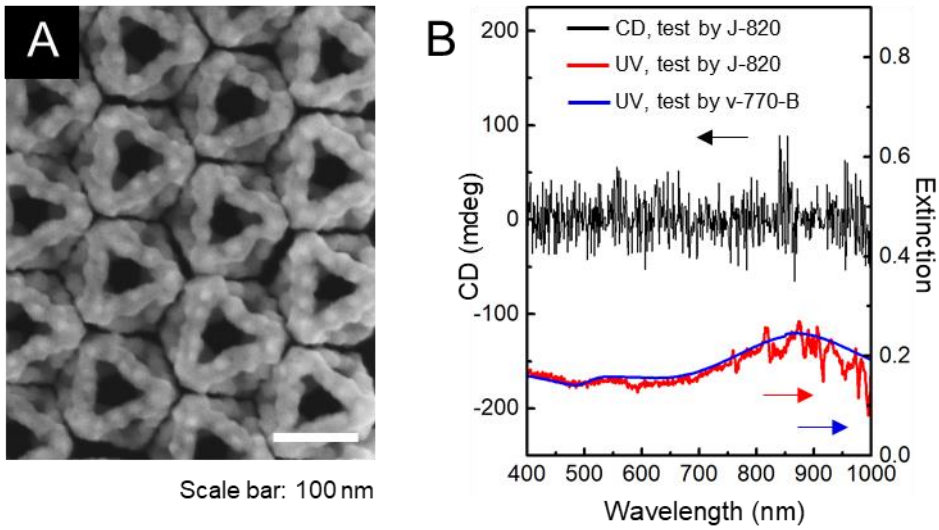


**Figure 4.6** SEM image and CD spectra of the s-c-Au ONF induced growth by L-Gsh (32 μM). The scale bar is 100 nm.

## 4.4 Conclusion

Overall, the successful preparation of seed Au NOF for chiral growth has been accomplished. SEM and the corresponding extinction spectra have revealed the morphology and uniformity of colloidal particles at various stages. However, the current chiral spectra did not show clear chiral activity, suggesting that the transition from Au NOF to c-Au NOF is evidently challenging. Seeds (with well-defined crystal planes) or growth conditions, such as gold precursor ($Au^{3+}$), strong chiral ligand (L-Gsh), weak ligand (CTAB) and mild reducing agent ascorbic acid are important for achieving precise chiral growth. In future studies, I will be aiming to further explore and optimize this work.

## 4.5 References


[1] Sun, L.; Tao, Y.; Yang, G.; Liu, C.; Sun, X.; Zhang, Q. Geometric Control and Optical Properties of Intrinsically Chiral Plasmonic Nanomaterials. *Adv. Mater.* **2023**, 2306297

[2] Im, S. W.; Ahn, H. Y.; Kim, R. M.; Cho, N. H.; Kim, H.; Lim, Y. C.; Lee, H. E.; Nam, K. T. Chiral Surface and Geometry of Metal Nanocrystals. *Adv. Mater.* **2019**, *32*, 1905758.

[3] Lee, H.-E.; Ahn, H.-Y.; Mun, J.; Lee, Y. Y.; Kim, M.; Cho, N. H.; Chang, K.; Kim, W. S.; Rho, J.; Nam, K. T. Amino-Acid- and Peptide-Directed Synthesis of Chiral Plasmonic Gold Nanoparticles. *Nature* **2018**, *556*, 360-365.

[4] Greber, T.; Šljivančanin, Ž.; Schillinger, R.; Wider, J.; Hammer, B. Chiral Recognition of Organic Molecules by Atomic Kinks on Surfaces. *Phys. Rev. Lett.* **2006**, *96*, 056103.

[5] Zhang, N.-N.; Shen, Z.-L.; Gao, S.-Y.; Peng, F.; Cao, Z.-J.; Wang, Y.; Wang, Z.; Zhang, W.; Yang, Y.; Liu, K.; Sun, T. Synthesis and Plasmonic Chiroptical Properties of Double-Helical Gold Nanorod Enantiomers. *Adv. Opt. Mater.* **2023**, *11*, 2203119.

[6] Ni, B.; Mychinko, M.; Gomez-Grana, S.; Morales-Vidal, J.; Obelleiro-Liz, M.; Heyvaert, W.; Vila-Liarte, D.; Zhuo, X.; Albrecht, W.; Zheng, G.; Gonzalez-Rubio, G.; Taboada, J. M.; Obelleiro, F.; Lopez, N.; Perez-Juste, J.; Pastoriza-Santos, I.; Coelfen, H.; Bals, S.; Liz-Marzan, L. M. Chiral Seeded Growth of Gold Nanorods Into Fourfold Twisted Nanoparticles with Plasmonic Optical Activity. *Adv. Mater.* **2023**, *35*, 2208299.

[7] Chen, J.; Gao, X.; Zheng, Q.; Liu, J.; Meng, D.; Li, H.; Cai, R.; Fan, H.; Ji, Y.; Wu, X. Bottom-up Synthesis of Helical Plasmonic Nanorods and Their Application in Generating Circularly Polarized Luminescence. *ACS Nano* **2021**, *15*, 15114-15122.

[8] Tao, Y.; Sun, L.; Liu, C.; Yang, G.; Sun, X.; Zhang, Q. Site-Selective Chiral Growth of Anisotropic Au Triangular Nanoplates for Tuning the Optical Chirality. *Small* **2023**, *19*, 2301218.

[9] Zheng, Y. L.; Wang, Q.; Sun, Y. W.; Huang, J.; Ji, J.; Wang, Z. J.; Wang, Y. W.; Chen, H. Y. Chiral Active Surface Growth via Glutathione Control. *Adv. Opt. Mater.* **2023**, *11*, 2202858.

[10] Ma, Y.; Cao, Z.; Hao, J.; Zhou, J.; Yang, Z.; Yang, Y.; Wei, J. Controlled Synthesis of Au Chiral Propellers from Seeded Growth of Au Nanoplates for Chiral Differentiation of Biomolecules. *J. Phys. Chem. C* **2020**, *124*,

24306-24314.

[11] Im, S. W.; Jo, E.; Kim, R. M.; Han, J. H.; Nam, K. T. 32-Symmetric Chiral Gold Nanoplates with Near-Infrared Circular Dichroism. *Adv. Opt. Mater.* **2023**, *11* 2300037.

[12] Zheng, J.; Boukouvala, C.; Lewis, G. R.; Ma, Y.; Chen, Y.; Ringe, E.; Shao, L.; Huang, Z.; Wang, J. Halide-Assisted Differential Growth of Chiral Nanoparticles with Threefold Rotational Symmetry. *Nat. Commun.* **2023**, *14*, 3783.

[13] González-Rubio, G.; Mosquera, J.; Kumar, V.; Pedrazo-Tardajos, A.; Llombart, P.; Solís, D. M.; Lobato, I.; Noya, E. G.; Guerrero-Martínez, A.; Taboada, J. M.; Obelleiro, F.; MacDowell, L. G.; Bals, S.; Liz-Marzán, L. M. Micelle-Directed Chiral Seeded Growth on Anisotropic Gold Nanocrystals. *Science* **2020**, *368*, 1472-1477.

[14] Kim, J. Y.; Yeom, J.; Zhao, G.; Calcaterra, H.; Munn, J.; Zhang, P.; Kotov, N. Assembly of Gold Nanoparticles into Chiral Superstructures Driven by Circularly Polarized Light. *J. Am. Chem. Soc.* **2019**, *141*, 11739-11744.

[15] Zheng, G.; He, J.; Kumar, V.; Wang, S.; Pastoriza-Santos, I.; Pérez-Juste, J.; Liz-Marzán, L. M.; Wong, K.-Y. Discrete Metal Nanoparticles with Plasmonic Chirality. *Chem. Soc. Rev.* **2021**, *50*, 3738-3754.

[16] Chung, P. J.; Lyu, L. M.; Huang, M. H. Seed-Mediated and Iodide-Assisted Synthesis of Gold Nanocrystals with Systematic Shape Evolution from Rhombic Dodecahedral to Octahedral Structures. *Chem. - Eur. J.* **2011**, *17*, 9746-9752.

[17] Jang, H. J.; Ham, S.; Acapulco, J. A., Jr.; Song, Y.; Hong, S.; Shuford, K. L.; Park, S. Fabrication of 2D Au Nanorings with Pt Framework. *J. Am. Chem. Soc.* **2014**, *136*, 17674-17680.

[18] Jung, I.; Kim, J.; Lee, S.; Park, W.; Park, S. Multiple Stepwise Synthetic Pathways toward Complex Plasmonic 2D and 3D Nanoframes for Generation of Electromagnetic Hot Zones in a Single Entity. *Acc. Chem. Res.* **2023**, *56*, 270-283.

[19] Wang, G.; Liu, Y.; Gao, C.; Guo, L.; Chi, M.; Ijiro, K.; Maeda, M.; Yin, Y. Island Growth in the Seed-Mediated Overgrowth of Monometallic Colloidal Nanostructures. *Chem* **2017**, *3* , 678-690.

[20] Yoo, S.; Kim, J.; Kim, J. M.; Son, J.; Lee, S.; Hilal, H.; Haddadnezhad, M.; Nam, J. M.; Park, S. Three-Dimensional Gold Nanosphere Hexamers Linked with Metal Bridges: Near-Field Focusing for Single Particle Surface Enhanced Raman Scattering. *J. Am. Chem. Soc.* **2020**, *142*, 15412-15419.

[21] Lee, H.-E.; Yang, K. D.; Yoon, S. M.; Ahn, H.-Y.; Lee, Y. Y.; Chang, H.; Jeong, D. H.; Lee, Y.-S.; Kim, M. Y.; Nam, K. T. Concave Rhombic Dodecahedral Au Nanocatalyst with Multiple High-Index Facets for $CO_2$ Reduction. *ACS Nano* **2015**, *9*, 8384-8393.

[22] Kim, J.; Hilal, H.; Haddadnezhad, M.; Lee, J.; Park, W.; Park, W.; Lee, J. W.; Jung, I.; Park, S. Plasmonic All-Frame-Faceted Octahedral Nanoframes with Eight Engraved Y-Shaped Hot Zones. *ACS Nano* **2022**, *16* , 9214-9221.

[23] Jang, H.-J.; Hong, S.; Ham, S.; Shuford, K. L.; Park, S. Site-Specific Growth of a Pt Shell on Au Nanoplates: Tailoring Their Surface Plasmonic Behavior. *Nanoscale* **2014**, *6*, 7339-7345.

[24] Yoo, S.; Go, S.; Son, J.; Kim, J.; Lee, S.; Haddadnezhad, M.; Hilal, H.; Kim, J. M.; Nam, J. M.; Park, S. Au Nanorings with Intertwined Triple Rings. *J. Am. Chem. Soc.* **2021**, *143*, 15113-15119.

[25] Zhang, N.-N.; Sun, H.-R.; Liu, S.; Xing, Y.-C.; Lu, J.; Peng, F.; Han, C.-L.; Wei, Z.; Sun, T.; Yang, B.; Liu, K. Gold Nanoparticle Enantiomers and Their Chiral-Morphology Dependence of Cellular Uptake. *CCS Chem.* **2022**, *4*, 660-670.

[26] He, B.; Wang, Y.; Zhang, M.; Xu, Y.; Zheng, Y.; Liu, X.; Wang, H.; Chen, H. Serrated Au Nanoplates via the Sharpening Etching Mode. *Chem. Mater.* **2022**, *34*, 8213-8218.

[27] Feng, Y.; Wang, Y.; Song, X.; Xing, S.; Chen, H. Depletion Sphere: Explaining the Number of Ag Islands on Au Nanoparticles. *Chem. Sci.* **2017**, *8*, 430-436.

# *Chapter 5*

## *General Conclusion*

## 5.1 General Conclusion

This thesis primarily presents a study on controlling the plasmonic chiroptical properties through meticulous design of particle structures. Firstly, by constructing a metal-molecule-metal core-gap-shell structure, I confirm that the enhancement of chiroptical response can be achieved through the strong coupling between chiral molecules in nanogaps or nanocavities and the enhanced near-field electromagnetic field within hot-spots. Secondly, by coating the surface of the structure with an active dielectric layer and subjecting it to pH and potential stimuli, the results demonstrate that the modulation of chiroptical response can be realized through changes in the external dielectric environment. These research findings provide further insights into understanding and manipulating the chiroptical properties of gold nanostructures.

The next challenge will focus on the development and optical tuning of intrinsic chiral nanoparticles and assemblies. This is because the progressive scale of asymmetry will bound to impart the system with more pronounced chiroptical properties, favouring the realization of further translation to applications. Despite numerous reports on chiral growth using simple-shaped particles as seeds, the corresponding relationship between the chiroptical properties and the geometric morphology of the particles has not been clearly established. This may necessitate a more comprehensive consideration of complex and multi-level particles. To address this, I introduced a well-defined gold octahedral nanoframe as the seed for chiral growth. Current research has obtained preliminary insights into the distorted morphology of the particle surface. The specific chiroptical properties will be further controlled through the optimization of geometric parameters.

In summary, this paper proposed a gold nanostructure for amplifying and dynamically tuning plasmonic chiroptical properties. The explicit design of the structure provides an open platform for flexible and rational tailoring of plasmonic cores, chiral molecules, and variable dielectrics to chiroptical needs, which is important for realizing applications in chemical sensing, chiral nanocatalysis, enantioselective separations, and novel optical devices.

## Publication

1. Han Lin, Hideyuki Mitomo, Yusuke Yonamine, Zhiyong Guo, Kuniharu Ijiro. Core–Gap–Shell Nanoparticles@ Polyaniline with Tunable Plasmonic Chiroptical Activities by pH and Electric Potential Dual Modulation. *Chemistry of Materials*, **2022**, 34, 9, 4062-4072.

## Presentation in Conferences

1. Han Lin, Hideyuki Mitomo, Zhiyong Guo, Kuniharu Ijiro
   Gold Nanostructures@Polyaniline with Tunable Switching Electrochemical Plasmonic Chiroptical Activities
   The 22nd Ries-Hokudai International Symposium, 12/2021, Online, Japan

2. Han Lin, Hideyuki Mitomo, Yusuke Yonamine, Zhiyong Guo, Kuniharu Ijiro
   Gold Nanostructures@Polyaniline with Tunable Dual Switching Plasmonic Chiroptical Activities
   The 20th Conference of the Nanosociety, 5/2022, Online, Japan

3. Han Lin, Hideyuki Mitomo, Yusuke Yonamine, Zhiyong Guo, Kuniharu Ijiro
   pH and Electrical Potential Dual-Responsive Chiral Plasmonic Nanoparticles
   The 8th Hokkaido University Cross-Departmental Symposium, 10/2022, Sapporo, Japan

4. Han Lin, Hideyuki Mitomo, Yusuke Yonamine, Zhiyong Guo, Kuniharu Ijiro
   Discrete Chiral Gold Nanorods with Tunable Chiroptical Activities by pH and Electric Potential Dual Modulation
   The 14th Asia-Pacific Conference on Near-field Optics, 6/2023, Busan, Korea

5. Han Lin, Hideyuki Mitomo, Yusuke Yonamine, Zhiyong Guo, Kuniharu Ijiro
   Tunable Chiroptical Activities of Discrete Chiral Gold Nanorods by pH and Electric Potential Dual Modulation
   The 14th ISAJ Annual Symposium on Integrated Science for a Sustainable Society, 11/2023, Sapporo, Japan